

Triple oxygen and clumped isotopes in modern soil carbonate along an aridity gradient in the Serengeti, Tanzania

Emily Beverly¹, Naomi E Levin², Benjamin H Passey², Phoebe G Aron², Drake A Yarian², Mara Page², and Elise M Pelletier²

¹University of Houston

²University of Michigan

November 24, 2022

Abstract

The isotopic composition of paleosol carbonates are used extensively to reconstruct past vegetation, climate, and altimetry, but poor constraints on soil evaporation and temperature have limited the utility of oxygen isotopes in the studies. Recent advances in carbonate clumped isotope thermometry ($T_{\text{cl}}[47]$) allow for independent controls on temperature, but the influence of evaporation remains unresolved. However, the sensitivity of 18O-17O-16O distributions to kinetic fractionation makes it possible to use triple oxygen isotopes ($[^{17}\text{O}]/^{16}\text{O}$) to track evaporation in water. Recent work shows the sensitivity of $[^{17}\text{O}]/^{16}\text{O}$ to evaporation in lakes and lacustrine carbonates, but little is known about variation of $[^{17}\text{O}]/^{16}\text{O}$ in soil carbonates and their potential to track evaporation. For this study, we sampled soils across an aridity gradient in the Serengeti, Tanzania to evaluate how soil carbonate $[^{17}\text{O}]/^{16}\text{O}$ tracks soil water evaporation. Modern soil carbonates were collected from 11 sites across a transect of the Serengeti Ecosystem where mean annual precipitation and aridity index range from 499 to 846 mm yr⁻¹ and 0.33 to 0.55, respectively. $\delta^{13}\text{C}$ values range from -2.7 to 1.8‰ dominated grasslands, whereas $\delta^{18}\text{O}$ values of soil carbonates vary by ~ 8 ‰. Carbonates average 23°C ($1\sigma \pm 4^\circ\text{C}$), which does not vary significantly across sites or with depth, likely due to minimal annual variation in temperature at the equator. Using these temperatures for each carbonate, reconstructed $\delta^{18}\text{O}$ values of soil water are up to 6‰ values of local precipitation and springs, indicating considerable soil water evaporation. The $[^{17}\text{O}]/^{16}\text{O}$ values of these soil carbonates range from -162 to -106 per meg and decrease as both aridity and $\delta^{18}\text{O}$ values increase. Our results support the hypothesis that soil water evaporation drives the variance in $\delta^{18}\text{O}$ and $[^{17}\text{O}]/^{16}\text{O}$ of soil carbonate in arid climates, demonstrating the potential for soil carbonate $[^{17}\text{O}]/^{16}\text{O}$ to track paleoaridity and constrain interpretations of paleosol carbonate $\delta^{18}\text{O}$ records.

1 **Title:** Triple oxygen and clumped isotopes in modern soil carbonate along an aridity gradient in
2 the Serengeti, Tanzania

3
4 **Authors:** Emily J. Beverly^{1,2}, Naomi E. Levin², Benjamin H. Passey², Phoebe G. Aron², Drake
5 A. Yarian², Mara Page², and Elise M. Pelletier²

6
7 ¹University of Houston
8 Earth and Atmospheric Sciences
9 3507 Cullen Blvd, Room 214
10 Houston, TX 77204 USA

11
12 ²University of Michigan
13 Department of Earth & Environmental Sciences
14 1100 North University Ave
15 Ann Arbor, MI 48109 USA

16
17 **Abstract**

18 The isotopic composition of paleosol carbonates are used extensively to reconstruct past
19 vegetation, climate, and altimetry, but poor constraints on soil evaporation and temperature have
20 limited the utility of oxygen isotopes in the studies. Recent advances in carbonate clumped
21 isotope thermometry ($T_{\Delta 47}$) allow for independent controls on temperature, but the influence of
22 evaporation remains unresolved. However, the sensitivity of ^{18}O - ^{17}O - ^{16}O distributions to kinetic
23 fractionation makes it possible to use triple oxygen isotopes ($\Delta^{17}\text{O}$) to track evaporation in
24 water. Recent work shows the sensitivity of $\Delta^{17}\text{O}$ to evaporation in lakes and lacustrine
25 carbonates, but little is known about variation of $\Delta^{17}\text{O}$ in soil carbonates and their potential to
26 track evaporation. For this study, we sampled soils across an aridity gradient in the Serengeti,
27 Tanzania to evaluate how soil carbonate $\Delta^{17}\text{O}$ tracks soil water evaporation. Modern soil
28 carbonates were collected from 11 sites across a transect of the Serengeti Ecosystem where mean
29 annual precipitation and aridity index range from 499 to 846 mm yr⁻¹ and 0.33 to 0.55,
30 respectively. $\delta^{13}\text{C}$ values range from -2.7 to 1.8‰ and reflect C₄ dominated grasslands, whereas
31 $\delta^{18}\text{O}$ values of soil carbonates vary by ~8‰ along a gradient in aridity. $T_{\Delta 47}$ from these soil

32 carbonates average 23°C (1σ ±4°C), which does not vary significantly across sites or with depth,
33 likely due to minimal annual variation in temperature at the equator. Using these temperatures
34 for each carbonate, reconstructed δ¹⁸O values of soil water are up to 6‰ higher than δ¹⁸O values
35 of local precipitation and springs, indicating considerable soil water evaporation. The Δ¹⁷O
36 values of these soil carbonates range from -162 to -106 per meg and decrease as both aridity and
37 δ¹⁸O values increase. Our results support the hypothesis that soil water evaporation drives the
38 variance in δ¹⁸O and Δ¹⁷O of soil carbonate in arid climates, demonstrating the potential for soil
39 carbonate Δ¹⁷O to track paleoaridity and constrain interpretations of paleosol carbonate δ¹⁸O
40 records.

41
42

43 **Keywords**

44 pedogenic carbonate, clumped isotopes, triple oxygen isotopes, evaporation, soil temperature,
45 Africa

46
47

48 **Text**

49
50

50 **1. Introduction**

51 Oxygen and carbon isotopes in pedogenic carbonates are used extensively for
52 reconstructions of past climates, environments, and elevations (e.g., Cerling et al., 2011;
53 Garzzone et al., 2008; Levin et al., 2011; Lüdecke et al., 2018; Rech et al., 2019). The carbon
54 isotope composition of soil carbonates (δ¹³C_{sc}) reflects the proportion of C₃ vs. C₄ plants
55 growing in the soil (Cerling et al., 2011). Interpretations of oxygen isotopes in soil carbonates are
56 less straightforward because δ¹⁸O values of soil carbonate (δ¹⁸O_{sc}) depend on both soil
57 temperature and isotopic composition of water associated with carbonate formation, which can
58 vary with the seasonality of soil carbonate formation, ambient temperatures, vegetation cover,
59 δ¹⁸O values of precipitation, and the degree of soil water evaporation (Breecker et al., 2009;

60 Kelson et al., 2020). Carbonate clumped isotope thermometry (Δ_{47}) has greatly advanced the
61 understanding of how soil temperature and the seasonality of carbonate formation influence
62 $\delta^{18}\text{O}_{\text{sc}}$ values (Passey et al., 2010; Quade et al., 2013), but many paleoclimate and paleoaltimetry
63 studies are still hampered by the inability to control for the effects of evaporation on $\delta^{18}\text{O}_{\text{sc}}$
64 values (e.g., Garziona et al., 2008; Rech et al., 2019).

65 Recent work shows that triple oxygen isotope (^{16}O , ^{17}O , and ^{18}O) distributions in waters
66 (leaves, lakes, and ponds) and the rock record (carbonates, sulfates, silicates, oxides) are
67 sensitive to evaporation (Bao et al., 2016; Gázquez et al., 2018; Li et al., 2017; Passey et al.,
68 2014; Passey and Ji, 2019; Surma et al., 2018). Although we know that evaporation plays a
69 strong role in soil carbonates, especially in hyper-arid environments where $\delta^{18}\text{O}_{\text{sc}}$ values are
70 often much greater than predicted using local temperatures and $\delta^{18}\text{O}$ of meteoric water ($\delta^{18}\text{O}_{\text{mw}}$)
71 (e.g., Quade et al., 2007), we currently do not have an independent way to gage soil water
72 evaporation in the rock record. There is tremendous potential to use $\Delta^{17}\text{O}$ in soils to evaluate the
73 effects of evaporation on $\delta^{18}\text{O}_{\text{sc}}$ values and assess past aridity, but we first need to understand
74 $\Delta^{17}\text{O}$ variation in modern soils before using it in the geologic record.

75 Here we present *in situ* measurements of soil temperatures and isotopic data from modern
76 soil waters ($\delta^{18}\text{O}_{\text{sw}}$, $\delta\text{D}_{\text{sw}}$, $\Delta^{17}\text{O}_{\text{sw}}$) and soil carbonates ($\delta^{13}\text{C}_{\text{sc}}$, $\delta^{18}\text{O}_{\text{sc}}$, $\Delta^{17}\text{O}_{\text{sc}}$, Δ_{47}) collected
77 along a northwest-southeast transect across the Serengeti Ecosystem of northern Tanzania (Fig.
78 1). This transect adds critical data to oxygen and carbon isotopic systematics of modern soils in
79 eastern Africa, which are understudied, despite the widespread application of paleosols
80 carbonates as indicators of paleoenvironment and paleoclimate (e.g., Cerling et al., 2011; Levin
81 et al., 2011; Lüdecke et al., 2018). We use these results to show how $\Delta^{17}\text{O}$ of soil carbonates
82 tracks local aridity in the Serengeti and demonstrate the potential for using the combination of

83 Δ_{47} and $\Delta^{17}\text{O}$ measurements to place firm constraints on how soil water evaporation affects
84 paleosol carbonate $\delta^{18}\text{O}$ records.

85

86 2. Isotope Notation

87 Stable isotopes of carbon and oxygen are reported using standard δ -notation,

$$88 \quad \delta = \left(\frac{R_x}{R_{std}} - 1 \right) 1000 \quad (1)$$

89 where R is the ratio of the abundance of the heavy to light isotope, x indicates the sample and std
90 is the standard.

91 The isotopic fractionation factor between any two substances (A and B) is defined as

$$92 \quad \alpha_{A-B} = \frac{R_A}{R_B}$$

93 where R is the isotope ratio (heavy to light) of a material. The mass-dependent isotopic
94 fractionation for $^{17}\text{O}/^{16}\text{O}$ and $^{18}\text{O}/^{16}\text{O}$ follows a power law relationship (Young et al., 2002):

$$95 \quad {}^{17}\alpha_{A-B} = {}^{18}\alpha_{A-B}^\theta \quad (2)$$

96 where θ is the fractionation exponent. This exponential relationship is linearized using
97 δ' -notation,

$$98 \quad \delta'_A = 1000 \ln \left(\frac{R_A}{R_{std}} \right) \quad (3)$$

99 such that the isotopic composition of A and B can be expressed as

$$100 \quad \overline{\delta'^{17}\text{O}} = \theta * \overline{\delta'^{18}\text{O}} \quad (4)$$

101 (Miller, 2002). $\Delta^{17}\text{O}$ is the deviation from this linear relationship, defined by a reference slope
102 λ_{ref}

$$103 \quad \overline{\Delta^{17}\text{O}} = \overline{\delta'^{17}\text{O}} - \lambda_{ref} \overline{\delta'^{18}\text{O}} \quad (5)$$

104 Hydrological studies typically define $\lambda_{ref} = 0.528$ (Fig. S1A), which roughly approximates the
 105 value of θ for equilibrium fractionation in waters (Luz and Barkan, 2010). This slope also
 106 approximates the relationship between $\delta^{18}\text{O}$ and $\delta^{17}\text{O}$ in meteoric waters globally, although it is
 107 heavily weighted towards polar samples and few data are available from the tropics (Aron et al.,
 108 in review; Luz and Barkan, 2010).

109 Clumped isotope thermometry uses Δ_i to represent the excess of an isotopologue, i ,
 110 relative to the expected stochastic distribution. Calculating the temperature-dependent mass-47
 111 anomaly (Δ_{47}) relative to the stochastic distribution is defined as:

$$112 \quad \Delta_{47} = \left[\left(\frac{R^{47}}{R^{47*}} - 1 \right) - \left(\frac{R^{46}}{R^{46*}} - 1 \right) - \left(\frac{R^{45}}{R^{45*}} - 1 \right) \right] * 1000 \quad (6)$$

113 where

$$114 \quad R^i = \frac{\text{mass } i}{\text{mass } 44} \quad (7)$$

115 R^{i*} is similar to R^i but corresponds to the ratio of the sample with a stochastic distribution
 116 (Kelson et al., 2020; Passey et al., 2010; Wang et al., 2004).

117

118 3. Study Area

119 Soil samples were collected from the Serengeti Ecosystem, which is defined as the area
 120 covered by the wildebeest migration. The Serengeti straddles the Tanzania-Kenya border and
 121 covers an area $\sim 24,000 \text{ km}^2$ (Reed et al., 2009). Soil maps indicate that almost all the soils
 122 contain pedogenic carbonate (de Wit, 1978; Jager, 1982). These soils cover a rainfall gradient of
 123 ~ 400 to 1200 mm yr^{-1} that extends from the southeast to northwest across the Serengeti (Reed et
 124 al., 2009). Seasonal variation in rainfall is primarily controlled by variations of the Intertropical
 125 Convergence Zone (ITCZ), which creates a short, warm dry season from December to February

126 and a longer, cooler dry season from June to October (Reed et al., 2009; Yin and Nicholson,
127 1998).

128

129 **4. Materials and Methods**

130 *4.1. Field Methods*

131 We sampled soils across the Serengeti in a transect from NW to SE to capture the greatest
132 range in mean annual precipitation (MAP) amounts and evaporation conditions while limiting
133 changes in vegetation (Fig. 1; Table 1). We collected samples from grasslands in intervals of ~25
134 km across the transect and additional samples from more woody environments were collected as
135 time permitted. Eleven sites are described using standard protocols for field description and
136 horizon designation (Soil Survey Staff, 2014) and then sampled for pedogenic carbonates and
137 soil waters. We sampled pedogenic carbonates at depth intervals of 20 cm where present and
138 focused on hard pedogenic carbonate nodules and coatings/pendants because they are better
139 analogues for carbonates sampled in the rock record. In the lab, the pedogenic carbonates were
140 cracked open and drilled or completely pulverized when the sample size was too small for the
141 amount of carbonate needed for both triple oxygen and clumped isotope analyses (~130 mg).

142 We collected soil samples for cryogenic vacuum distillation of soil waters at ~20 cm
143 depth intervals in soil pits using glass vials sealed with a rubber stopper and wrapped in parafilm.
144 These samples represent a seasonal snapshot of soil water as they were sampled during the
145 shorter, warmer dry season in February 2018. Water samples collected from nearby lakes, rivers,
146 springs, and groundwater, were filtered using 0.45 μm PTFE filters in the field. All waters were
147 treated with activated charcoal for 24 hours to remove organic contaminants in the lab (West et
148 al., 2006).

149 We collected soil temperature data from four sites in the Serengeti National Park using
150 nine HOBO 64K Pendant® temperature loggers buried at the following depths: Ndabaka (20, 80,
151 and 150 cm depth), Musabi (40 and 140 cm depth), Kemarishe (30 and 100 cm depth), and Naabi
152 Hill (20, 90, and 150 cm depth) (Fig. 1). These loggers have a quoted accuracy of $\pm 0.53^\circ\text{C}$. Due
153 to permitting issues, it was not possible to bury temperature loggers in the Ngorongoro
154 Conservation Area, and therefore no data are available from the Malambo Road or Shifting
155 Sands sites (Fig. 1). Data are trimmed to 2-22-2018 to 1-26-2019 with a start date 2 days after
156 last logger was buried to allow soil temperatures to equilibrate (Table S1).

157 4.2. Soil Temperature Modeling

158 We modeled soil temperature as a function of time (t) and depth (z) using the following
159 equation:

$$160 \quad T(z, t) = T_{avg} + A_o \left[\sin \left(\omega t - \frac{z}{d} \right) \right] / e^{z/d} \quad (8)$$

161 where T_{avg} is average soil temperature, A_o is the amplitude of seasonal temperature variation at
162 the soil surface, ω is the radial frequency ($2\pi \text{ year}^{-1}$), z is depth from soil surface, and d is the
163 “damping depth” which is related to the thermal properties of the soil and frequency of
164 temperature fluctuations (Shukla, 2014). This is given by the equation:

$$165 \quad d = \left(\frac{2\kappa}{C_v \omega} \right)^{1/2} \quad (9)$$

166 where κ is the thermal conductivity and C_v is the volumetric heat capacity (Shukla, 2014). For
167 this model, we assigned T_{avg} as mean annual air temperature (MAAT) at the surface and
168 calculated A_o using the average temperature of the warmest and coldest month from Fick and
169 Hijmans (2017). We explored the effects of using the full range of values for κ and C_v , which can
170 vary with soil texture and water content (Shukla, 2014), on damping depth and modeled
171 temperatures but the impacts were almost imperceptible. Therefore, our calculations of damping

172 depth use average values of κ (1.02 W/m³/°K) and C_v (2.08 J/m³/°K) reported by Shukla (2014).
173 Traditionally, this soil temperature model is used for environments at higher latitudes with four
174 temperature seasons over one annual revolution (i.e., 2π year⁻¹), but equatorial Africa has only
175 two distinct temperature peaks in a year. For this reason, we double the radial frequency (ω),
176 which is the rate of change of phase of the sinusoidal waveform used to represent annual
177 temperature fluctuations, to simulate two temperature peaks per year.

178 *4.3. Stable Isotope Measurements*

179 All stable isotope measurements were made at the University of Michigan. Water δ D and
180 δ^{18} O were analyzed on a Picarro L2130-i cavity ringdown spectrometer with an A0211
181 high-precision vaporizer and attached autosampler. Each sample was analyzed 10 times; we
182 report the average of the last 5 analyses. The Picarro ChemCorrect software was used to monitor
183 samples for organic contamination and normalized measured δ^{18} O and δ D to the VSMOW-SLAP
184 scale with USGS reference waters (USGS45, 46, 49, and 50) and four in-house liquid standards.
185 Precision of repeat analyses of deionized water was better than 0.1‰ and 0.3‰ for δ^{18} O and δ D,
186 respectively. Soil waters were extracted using cryogenic vacuum distillation (West et al., 2006).

187 Carbon and oxygen stable isotope compositions (δ^{13} C_{sc} and δ^{18} O_{sc}) of powdered
188 carbonates were analyzed on a Nu Perspective isotope ratio mass spectrometer (IRMS) in the
189 Isotopologue Paleosciences Laboratory with an online Nu Carb autosampler and digested in
190 100% H₃PO₄ at 90°C. Corrections are based on a two-point calibration using the NBS-18 and
191 NBS-19 calcite standards and are reported using the standard δ -notation (Equation 1) relative to
192 VPDB in ‰ units (Table S2 and 3). Precision (1 σ , hereafter reported using \pm) for the standards
193 during the analytical interval for these unknowns was <0.02‰ for δ^{13} C and <0.05‰ for δ^{18} O.

194 Clumped isotope analyses of carbonates (Δ_{47}) were conducted using a custom built
195 device for the reaction of samples in 100% H_3PO_4 at 90°C and purification of the resultant CO_2
196 through multiple cryogenic traps and a gas chromatograph (GC) column at -20°C (Passey et al.,
197 2010). Isotope ratios of the stable CO_2 isotopologues were then analyzed on a Nu Perspective
198 IRMS. Δ_{47} values were normalized to the carbon dioxide equilibrium scale following Dennis et
199 al. (2011) and Δ_{47} temperatures ($T_{\Delta 47}$) were calculated using Equation 3 from Bonifacie et al.
200 (2017) based on 2 to 5 replicates (Tables S4, S5). The Δ_{47} standard error (SE) for each sample is
201 calculated using the SE from replicate analyses. We use the pooled standard deviation (σ_p) of
202 secondary reference standards to document the external reproducibility of replicates using
203 performance of ETH-1 to ETH-4, NBS-19, and three internal standards (102-GC-AZ01,
204 GON06-OES, and Hagit Carrara), which have a σ_p of 0.019‰ for Δ_{47} (Table S6). The
205 reconstructed oxygen isotope composition of the soil carbonate parent waters ($\delta^{18}\text{O}_{\text{rsw}}$) was
206 calculated using $T_{\Delta 47}$ and the calcite-water fractionation factor temperature equation by Kim and
207 O’Neil (1997). The error on the $\delta^{18}\text{O}_{\text{rsw}}$ is propagated from the error associated with $T_{\Delta 47}$. A few
208 samples with lower than expected temperatures for equatorial tropical soils were treated with 3%
209 H_2O_2 to remove organic contaminants. Treatment resulted in temperatures within error of the
210 untreated samples (Table S5).

211 The $^{18}\text{O}/^{16}\text{O}$ and $^{17}\text{O}/^{16}\text{O}$ ratios of water samples were measured on O_2 generated by
212 passing water through a 370°C cobalt (III) fluoride reactor and then analyzed using a Nu
213 Perspective IRMS at the University of Michigan. These methods are summarized in Li et al.
214 (2017) and have changed very little except that O_2 was previously analyzed on a Thermo 253
215 IRMS at Johns Hopkins University. The triple oxygen isotope composition of carbonate samples
216 were measured using the acid digestion-reduction-fluorination method (Passey et al., 2014).

217 Isotopic data from analyses of both water and carbonate were normalized to the VSMOW-SLAP
218 scale (Schoenemann et al., 2013), and results from the carbonate analyses were subjected to an
219 additional normalization step to correct for mass dependent fractionation in $\delta^{18}\text{O}$ and $\delta^{17}\text{O}$
220 detailed in Section 2.3 of Passey et al. (2014). This correction does not affect $\Delta^{17}\text{O}$ values
221 because the fractionation effects are mass-dependent with a slope that is not resolvable from λ_{ref}
222 = 0.528.

223 The precision for the triple oxygen isotope analyses of waters was determined using
224 performance of USGS45 (n=11), USGS50 (n=6), USGS47 (n=6), and GISP (n=4). Standard
225 deviations for $\delta^{18}\text{O}$, $\delta^{17}\text{O}$, and $\Delta^{17}\text{O}$ were <0.6‰, 0.3‰, and 15 per meg, respectively. During
226 the interval of time when these waters were analyzed, the σ_p was 0.5‰, 0.2‰, and 11 per meg
227 for $\delta^{18}\text{O}$, $\delta^{17}\text{O}$, and $\Delta^{17}\text{O}$, respectively. Carbonate precision for $\delta^{18}\text{O}$, $\delta^{17}\text{O}$, and $\Delta^{17}\text{O}$ was
228 evaluated using three standards NBS-19 (n=6), NBS-18 (n=3) and 102-GC-AZ01 (n=2; internal
229 standard). Standard deviations for $\delta^{18}\text{O}$, $\delta^{17}\text{O}$, and $\Delta^{17}\text{O}$ were <3.1‰, 1.6‰, and 4 per meg,
230 respectively. σ_p for the carbonate standards was 2.5‰, 1.3‰, and 3 per meg for $\delta^{18}\text{O}$, $\delta^{17}\text{O}$, and
231 $\Delta^{17}\text{O}$, respectively (Table S6). Subsequent analyses have shown that the precision for these
232 sessions is similar to the long-term, external precision of waters analyzed in the University of
233 Michigan system, which has a pooled standard deviation of USGS reference waters of 0.3‰,
234 0.5‰, and 8 per meg for $\delta^{17}\text{O}$, $\delta^{18}\text{O}$, and $\Delta^{17}\text{O}$, respectively (Aron et al., in review). See Tables
235 S6-S11 for the results and normalization approach for all analyses.

236

237 **5. Results**

238 *5.1. Soil Description and Temperatures*

239 Eleven soils sampled for this study include Inceptisols, Mollisols, and Alfisols (Table
240 S12, Figs. S2A-D). These USDA soil order classifications are only based on field description to
241 summarize the dominant features of each soil and do not include any laboratory analysis as the
242 carbonates were the focus of this study. At 9 of the 11 sites, pedogenic carbonate was identified,
243 which ranged in morphology from hard nodules to carbonate coatings and pendants to indurated
244 petrocalcic horizons. Representative examples of each type of soil carbonate morphology are
245 shown in Figure S2E-I.

246 Results from the HOBO[®] temperature loggers are shown in Figure 2A and represent a
247 11-month long log of soil temperature variation. Maximum soil temperatures, variance, and
248 standard deviation decrease with depth at each site and minimum temperatures increase with
249 depth (Table 2). The mean soil temperatures of these grassland soils decrease to the southeast in
250 the transect, similar to MAAT (Table 2; Figs. 1 and 2A) with the exception of Kemarishe, which
251 has the highest MAST of any of the soils measured. Results from the soil temperature modeling
252 are shown using two different depths (20 and 150 cm) from the warmest (Ndabaka) and coolest
253 site (Naabi Hill), which had temperature logger data available for comparison (Figs. 3A-D).
254 These results show that the soil temperature modeling generally follows the seasonal changes in
255 air temperature, which peaks twice yearly. The amplitude of temperature variation decreases
256 with increasing depth and temperatures at depth lag those closer to the surface.

257 5.2. Waters - $\delta^{18}\text{O}$, *d*-excess, and $\Delta^{17}\text{O}$

258 $\delta^{18}\text{O}$ values range from -5.0‰ to 10.4‰ (n=64), *d*-excess values range from -16.3 to
259 58.5‰, and $\Delta^{17}\text{O}$ values range from -24 to 25 per meg for water samples from springs, lakes,
260 rivers, pools, and precipitation (n=45; Table S13; Figs. 4B, 4C, and 5C). Soil waters (n=16)

261 range from -3.8 to 5.5‰ for $\delta^{18}\text{O}$ ($\delta^{18}\text{O}_{\text{sw}}$), -31.1 to 11.6‰ for d-excess ($\text{d-excess}_{\text{sw}}$), and -13 to
262 63 per meg for $\Delta^{17}\text{O}$ ($\Delta^{17}\text{O}_{\text{sw}}$) (Figs. 4B, 4C, 5A-D).

263 5.3. Carbonates - $\delta^{13}\text{C}$, $\delta^{18}\text{O}$, Δ_{47} , and $\Delta^{17}\text{O}$

264 We analyzed sixty-nine unique soil carbonate nodules from 9 sites (Table S2; Fig. 1) for
265 $\delta^{13}\text{C}$ and $\delta^{18}\text{O}$ to explore isotopic variation between sites, at different depths within a single
266 profile, and between nodules at each depth. Mean $\delta^{18}\text{O}_{\text{sc}}$ values range from -4.5‰ at Banagi to
267 4.3‰ at Shifting Sands, but there is no consistent trend with depth (Table S3; Fig. 6B). There is
268 no trend across the transect, but rather a step-wise increase in $\delta^{18}\text{O}_{\text{sc}}$ at the most arid sites,
269 Malambo Road and Shifting Sands. $\delta^{18}\text{O}_{\text{sc}}$ ranges from -0.98 to 4.3‰ at Malambo Road and
270 Shifting Sands, whereas $\delta^{18}\text{O}_{\text{sc}}$ values from all other sites range from -4.5 to -1.5‰. $\delta^{13}\text{C}_{\text{sc}}$
271 values of soil carbonates range from -2.7‰ at Musabi to 1.8‰ at Shifting Sands (Table S2; Fig.
272 6A). The relationships between $\delta^{13}\text{C}_{\text{sc}}$ values and depth vary among the sampling sites, with
273 some sites showing slight increases (e.g. Nyaruswiga) or decreases in $\delta^{13}\text{C}_{\text{sc}}$ values (e.g. Musabi,
274 Ndabaka, Naabi Hill), and others not varying at all (e.g. Simba Kopjes, Naabi Hill) (Table S2;
275 Fig 6C).

276 We selected a subset of these samples for Δ_{47} analysis (n=28), targeting at least one
277 sample from each depth in a soil profile where carbonate was present. At sites where carbonate
278 was only present at a single depth (i.e. Malambo Road, Shifting Sands, Banagi), we analyzed two
279 different samples from that depth. $T_{\Delta_{47}}$ from all carbonates sampled ranges from 14 to 31 °C
280 with an average of 23 ± 4 °C (Table S5; Fig. 2B). Only Ndabaka shows a trend between $T_{\Delta_{47}}$ and
281 soil depth, where $T_{\Delta_{47}}$ values range from 29 ± 6 °C at the top of the carbonate zone (70 cm) to 19
282 ± 3 °C at the base (130 cm). We calculated $\delta^{18}\text{O}_{\text{rsw}}$ using $T_{\Delta_{47}}$ and $\delta^{18}\text{O}_{\text{sc}}$ values and the
283 temperature dependent fractionation factor between water and carbonate under equilibrium

284 conditions (Kim and O'Neil, 1997). $\delta^{18}\text{O}_{\text{rsw}}$ values range from 1.1 to 5.9‰ at the most arid sites,
285 Malambo Road and Shifting sands and from -3.2 to 1.6‰ elsewhere. These calculations indicate
286 that higher $\delta^{18}\text{O}_{\text{sc}}$ values at more arid sites are not produced by changes in $T_{\Delta 47}$, but instead
287 reflect higher soil water $\delta^{18}\text{O}$ values (Fig. 7A).

288 We prioritized $\Delta^{17}\text{O}$ analysis of samples from sites that represented the full range of
289 environments (from semi-arid at Malambo and Shifting Sands to dry-subhumid at Ndabaka). We
290 analyzed samples from Simba Kopjes to represent an intermediate environment and because it
291 has carbonate at multiple depths. The $\Delta^{17}\text{O}$ values of soil carbonate ($\Delta^{17}\text{O}_{\text{sc}}$) range from -162 to
292 -106 per meg, with an average of -127 ± 20 per meg (Table S5). We calculate the $\Delta^{17}\text{O}$ of
293 reconstructed soil water ($\Delta^{17}\text{O}_{\text{rsw}}$) using $T_{\Delta 47}$, which provides the necessary temperature
294 information to calculate $^{18}\alpha$ ($\text{CaCO}_3\text{-H}_2\text{O}$) (Kim and O'Neil, 1997). $^{17}\alpha$ ($\text{CaCO}_3\text{-H}_2\text{O}$) is
295 calculated using the value for $^{18}\alpha$ in the following equation:

296
$$\boxed{^{17}\alpha = ^{18}\alpha^\lambda} \quad (10)$$

297 where λ is assumed to be 0.5245 (Fig. S1C; Passey et al., 2014). $\Delta^{17}\text{O}_{\text{rsw}}$ ranges from -31 to 20
298 per meg, with an average of 0 ± 21 per meg (Fig. S1C; Table S5).

299

300 **6. Discussion**

301 *6.1. Water Isotopes*

302 Despite a growing isotopic dataset from meteoric waters in eastern Africa (Bedaso et al.,
303 2020; Levin et al., 2009; Odada, 2001; Otte et al., 2017; Rozanski et al., 1996), we are not aware
304 of any $\delta^{18}\text{O}$ and δD data from meteoric waters for the Serengeti Ecosystem. The closest
305 systematic rainfall collections are from the Global Network for Isotopes in Precipitation (GNIP)
306 station in Nairobi, >200 km to the northeast, and on the slopes of Mt. Kilimanjaro, >250 km to

307 the southeast (Otte et al., 2017; Rozanski et al., 1996). The new $\delta^{18}\text{O}$ and δD values of the waters
308 from the Serengeti (Table S13; Figs. 4B and C) fall in the range of interpolated values from the
309 GNIP dataset (Fig. 4A; Bowen, 2020; Bowen and Revenaugh, 2003). $\Delta^{17}\text{O}$ data from African
310 waters are very limited, but surface and tap water data from Mpala, Kenya range from -16 to 24
311 per meg (Li et al. 2017) and range from -18 to 26 per meg for monsoonal precipitation from
312 Niger (Landais et al., 2010), similar to $\Delta^{17}\text{O}$ values of -25 to 23 per meg measured for this study
313 (Fig. 5A and C).

314 Grouping the data by water type, we observe that $\delta^{18}\text{O}$ and δD values of groundwater,
315 precipitation and springs plot on or close to the global, regional and local meteoric water lines
316 (Fig. 4B; Dansgaard, 1964; Otte et al., 2017; Rozanski et al., 1996), whereas pools, rivers, and
317 lakes from the Serengeti plot to the right of these meteoric water lines. These surface waters have
318 higher $\delta^{18}\text{O}$ values ($2.8 \pm 3.9\text{‰}$), lower d-excess values ($3.6 \pm 9.9\text{‰}$), and lower $\Delta^{17}\text{O}$ values (-3
319 ± 13 per meg) than isotopic values of groundwater, precipitation, and springs ($-2.8 \pm 2.2\text{‰}$; 16.8
320 $\pm 11.0\text{‰}$, 12 ± 10 per meg) (Figs. 4B, 4C, 5A, and 5C). This distinction indicates the role of
321 evaporation in modifying the isotopic composition of Serengeti surface waters. The waters were
322 collected in February 2018 during the shorter but hotter dry season (December to February),
323 when maximum evaporative water loss may be expected.

324 Soil waters are isotopically distinct from both surface waters and precipitation/spring
325 waters, yielding average $\delta^{18}\text{O}$, d-excess and $\Delta^{17}\text{O}$ values of $-0.9 \pm 2.3\text{‰}$, $-4.2 \pm 12.4\text{‰}$, and 14
326 ± 18 per meg (Figs. 4B, 4C, 5B and D), respectively. Like surface waters, soil waters plot to the
327 right of the meteoric water line and yield relatively low d-excess and $\Delta^{17}\text{O}$ values, indicating the
328 influence of evaporation. The effects evaporation on soil water has been observed in $\delta^{18}\text{O}$ and
329 δD values in modern soils (Hsieh et al., 1998) and experimentally demonstrated and modeled in

330 the laboratory (Allison et al., 1983; Barnes and Allison, 1983), though not previously
331 demonstrated for $\Delta^{17}\text{O}$. However, lower $\delta^{18}\text{O}$ values in soil waters than surface waters suggest
332 recharge at different times. Shifting Sands and Malambo Road were collected after a recent
333 storm, which is observed in the isotopic data and suggests that recent rains disproportionately
334 contributed to the soil water pool and are not representative of annually integrated soil water.
335 The $\delta^{18}\text{O}_{\text{sw}}$ values are ~ 2 to 4‰ lower at 20 cm than samples at 40 cm and the $d\text{-excess}_{\text{sw}}$ and
336 $\Delta^{17}\text{O}_{\text{sw}}$ are higher at the surface (~ 20 to 30‰ and 30 to 40 per meg, respectively) than those at
337 depth (Figs. S3A, C, and E).

338 *6.2. Measured, Modeled, and Clumped Isotope Soil Temperatures*

339 Soil temperature monitoring is an important component to understand the conditions of
340 soil carbonate formation in the Serengeti and to interpret our $T_{\Delta 47}$ results. Here we compare our
341 11-month logs of soil temperature to existing but limited air temperature and soil temperature
342 from the Serengeti. Mean Annual Soil Temperatures (MAST) for all depths range from 23 to
343 26°C for this study (Table 2). This is similar to existing records of MAAT (21°C) and MAST
344 (25°C , 50 cm depth) at Serengeti National Park, collected in 1975-1976 from the Serengeti
345 Research Institute located near the center of the Serengeti National Park (Jager, 1982). This is
346 also similar to MAAT values produced from spatial interpolations (Fick and Hijmans (2017),
347 which range from 19 to 22°C .

348 Our temperature monitoring in the Serengeti shows that soil temperature varies by
349 vegetation type such that grassland soils (Ndabaka, Musabi, and Naabi Hill) are cooler on
350 average than the grassed woodland soil (Kemarishe). For example, mean temperatures from the
351 lowest depths of each soil are statistically lower for Ndabaka ($26.40 \pm 0.35^\circ\text{C}$), Musabi ($25.90 \pm$
352 0.58°C), and Naabi Hill ($23.78 \pm 0.44^\circ\text{C}$) than those from Kemarishe ($26.73 \pm 0.78^\circ\text{C}$) (Tables 2

353 and S14; Fig. 2A). The mean temperatures from Kemarishe are the warmest among all the sites
354 and have the highest minimum temperatures and warmest maximum temperatures although
355 shaded woodlands are typically cooler than grasslands (Cerling et al., 2011). This may be due to
356 a local climate anomaly, water use differences between these sites, or a product of the
357 distribution of trees and shrubs at Kemarishe, which are not densely packed in a grassed
358 woodland.

359 Modeling of Serengeti soil temperatures indicates a 2 to 3°C range over the year, which
360 is similar to measured temperatures that vary from ~1 to 2.5°C at 150 cm depth (Table 2).
361 Limited variation in soil temperature is expected at the equator where variations in MAAT are
362 limited to ±4°C in the Lake Victoria Basin, which includes the Serengeti (Yin and Nicholson,
363 1998). Despite the similarity in amplitude, we note that modeled soil temperatures are 3 to 4°C
364 cooler than observed temperatures because this simple model does not account for ground
365 heating by incident solar radiation, which is significant in grassland soils that receive direct
366 sunlight (Fig. 2A; Quade et al., 2013) like the grassland soils in this study. Ground air
367 temperature increases with observed solar radiation by 1.21 K/100 W m⁻² (Bartlett et al., 2006).
368 The Lake Victoria Basin receives on average 412 W m⁻² of incident solar radiation (Yin and
369 Nicholson, 1998), which may increase temperature by up to 5°C in the Serengeti and may
370 explain the discrepancy of 3 to 4 °C between the modeled and measured soil temperatures (Figs.
371 3E and F). When we account for ground heating and add 5°C to our model results, the range of
372 modeled temperatures overlaps with most of the T_{Δ47} results and the range of measured soil
373 temperatures (Fig. 2B). The measured soil temperatures and modeling show very little
374 seasonality and likely explains why we observe little variation in T_{Δ47} by depth among

375 carbonates for these same soils, with the exception of Ndabaka, where temperature decreases
376 from 29 to 19 °C from 70 to 130 cm depth.

377 Overall, $T_{\Delta 47}$ of soil carbonates from the Serengeti range from 14 to 29°C with an
378 average of $23 \pm 4^\circ\text{C}$ and plot within the range of soil temperature measured over the 11-month
379 monitoring campaign (Fig. 2B). These Serengeti temperatures are similar to single $T_{\Delta 47}$
380 measurement of $18.8 \pm 1.6^\circ\text{C}$ from nearby Masai Mara Park, ~100 km north of the Serengeti
381 transect in Kenya (Passey et al., 2010). Data available from other parts of eastern Africa are
382 significantly warmer than the Serengeti by 5 to 10°C. Modern soil temperatures from the
383 Turkana region in northern Kenya have a mean of 35°C and maximum of 38°C at 50 cm depth
384 (Passey et al., 2010), which is >10°C warmer than any soils from the Serengeti. Soil
385 temperatures from the Afar region of Ethiopia are also warmer with a mean of 28°C and
386 maximum temperature of 29°C at ~50 cm depth for both grassland and wooded soils (Passey et
387 al., 2010). $T_{\Delta 47}$ values reconstructed from soil carbonates in the Afar range from 25 to 40°C and
388 are consistent with the range of measured soil temperatures (Passey et al., 2010). Further south in
389 the Karonga Basin near Lake Malawi, soil temperatures at 40 cm depth range from a mean of 27
390 $\pm 2.1^\circ\text{C}$ in partial shade to a mean of $31 \pm 3.2^\circ\text{C}$ in full sun (Lüdecke et al., 2018).

391 Soil carbonates can form in different periods throughout the year but primarily form
392 during the warm, dry season (Breecker et al., 2009; Kelson et al., 2020; Passey et al., 2010;
393 Quade et al., 2013), and for this reason most $\Delta 47$ studies of modern soil carbonates identify a
394 warm season bias in $T_{\Delta 47}$ (Kelson et al., 2020, and references therein). However, elevation likely
395 explains much of the difference in mean soil temperature between Turkana, Afar, and Karonga
396 (400 to 500 meters above sea level) and the Serengeti (1100 to 1600 masl). The lapse rate in
397 eastern Africa is $-5.8^\circ\text{C}/\text{km}$ (Loomis et al., 2017), and so the rest of this 5 to 10°C discrepancy

398 between the Serengeti and Turkana, Afar, and Karonga can likely be explained by a combination
399 of aridity and seasonality of temperature. The lowest measured soil temperatures in eastern
400 Africa occur in the Serengeti with the highest elevation and a MAP of 400 to 850 mm yr⁻¹. The
401 warmest temperatures occur in the Afar and Turkana at low elevations and low MAP (300 to 400
402 mm yr⁻¹). Karonga is at lower elevation but higher MAP (~1111 mm yr⁻¹) falls in between (Fick
403 and Hijmans, 2017).

404 *6.3. Carbonate Isotopes and Vegetation Relationships*

405 Despite the abundance of research on paleosol carbonates in Africa in conjunction with
406 paleoanthropological research (e.g., Cerling et al., 2011; Levin et al., 2011; Lüdecke et al.,
407 2018), there are few studies of modern African pedogenic carbonates. In Figure 6A, the gray dots
408 show all known modern $\delta^{13}\text{C}_{\text{sc}}$ and $\delta^{18}\text{O}_{\text{sc}}$ data available from the literature for Africa from
409 Libya, Morocco, and South Africa (n=51) and the black dots represent samples in eastern Africa
410 from Kenya, Tanzania, and Ethiopia (n=16) (Cerling and Quade, 1980; Passey et al., 2010;
411 Salomons et al., 1978).

412 The carbon isotope data from the Serengeti soils plot among the highest $\delta^{13}\text{C}_{\text{sc}}$ values
413 relative to other African modern soils and correspond to grassland vegetation with the exception
414 of three samples from Musabi. All sites were mapped as grassland vegetation with the exception
415 of Makoma (shrubland) and Kemarishe (woodland) (Reed et al., 2009), which did not have
416 pedogenic carbonate identified in the soil, and therefore no comparisons could be made. The
417 three exceptions from Musabi are classified as wooded grasslands, but the average $\delta^{13}\text{C}_{\text{sc}}$ for
418 Musabi is $-0.3 \pm 1.4\text{‰}$ (Table S3). This suggests that $\delta^{13}\text{C}_{\text{sc}}$ faithfully represents the vegetation of
419 the environments in which they form. In addition to the expected relationship with vegetation,
420 $\delta^{13}\text{C}_{\text{sc}}$ values should increase at the surface (<40 cm depth) due to interaction with an enriched

421 atmosphere and $\delta^{18}\text{O}_{\text{sc}}$ should increase towards the surface due to evaporative enrichment and
422 (Figs. 6B and C; Breecker et al., 2009). However, we did not observe these expected
423 relationships because there was no pedogenic carbonate > 40 cm at these sites.

424 *6.4. Relationship between $\Delta^{17}\text{O}_{\text{sc}}$ and Aridity*

425 The combination of $\delta^{18}\text{O}_{\text{sc}}$ and Δ_{47} data from the Serengeti indicate that $\delta^{18}\text{O}_{\text{rsw}}$ values for
426 some sites are considerably higher (8‰) than $\delta^{18}\text{O}$ values of local unevaporated waters
427 (precipitation, springs, groundwater) and indicate that these carbonates formed from waters that
428 experienced considerable evaporation (Fig. 7A). This is consistent with studies from other arid
429 regions, where $\delta^{18}\text{O}_{\text{rsw}}$ values are significantly higher than local $\delta^{18}\text{O}_{\text{mw}}$ values and attributed to
430 evaporation (Quade et al., 2007). In the Serengeti, enriched $\delta^{18}\text{O}_{\text{rsw}}$ values are only observed at
431 Malambo Road and Shifting Sands. Other sites plot within $\pm 2\%$ of the expected $\delta^{18}\text{O}_{\text{mw}}$ with the
432 exception of one sample from Simba Kopjes (Fig. 7A). There are no clear distinctions in
433 measured soil temperatures, $T_{\Delta 47}$, vegetation, or soil texture among these sites to explain these
434 elevated $\delta^{18}\text{O}_{\text{rsw}}$ values (Tables 1, S1, S5, and S12). The main distinguishing feature is the
435 climate of the sites.

436 We differentiate the climate of these sites in terms of aridity, using the aridity index (AI =
437 MAP/PET), where there are five broad climate classes: hyper arid, arid, semi-arid, dry
438 sub-humid, and humid (Middleton and Thomas, 1997). AI values for Malambo Road and
439 Shifting Sands plot as semi-arid (0.33-0.38), whereas the remaining sites yield higher AI values
440 (0.51-0.55) that cluster in the dry sub-humid category (Table 1; Fig. 7C). Another common
441 method of differentiating aridity uses water deficit (WD = PET-MAP) where high values
442 indicate a greater water deficit. Malambo Road and Shifting Sands similarly have a high WD of
443 963 to 1084 mm yr⁻¹ and all other sites range from 717 to 829 mm yr⁻¹ (Table 1; Fig. 7D).

444 The $\Delta^{17}\text{O}$ and $\delta^{18}\text{O}$ values of soil carbonates in the Serengeti track aridity. $\Delta^{17}\text{O}_{\text{rsw}}$
445 values are >50 per meg lower at semi-arid sites (Malambo Road, Shifting Sands) than at dry
446 sub-humid sites (Simba Kopjes, Ndabaka, and Banagi; Fig. 7C). We also observe a sharp
447 increase in $\delta^{18}\text{O}_{\text{rsw}}$ values from -4.4 to 6.1‰ with increased aridity (Fig. 7A and Table S5). A
448 single soil carbonate from Ndabaka (AI = 0.55), with a $\Delta^{17}\text{O}_{\text{rsw}}$ value of -11 per meg, is an
449 exception to this trend. It is the shallowest sample from this profile (70 cm depth) and the
450 combination of lower $\Delta^{17}\text{O}_{\text{rsw}}$ values and higher $\delta^{18}\text{O}_{\text{rsw}}$ values (Fig. 7B) likely reflect increased
451 evaporation of soil water closer to the surface (Fig. S4).

452 These data match our expectations for decreased $\Delta^{17}\text{O}$ and increased $\delta^{18}\text{O}$ values in
453 more arid sites where evaporation drives isotopic fractionation of soil water (Fig S1B). The
454 influence of evaporation on triple oxygen isotope composition of waters is well documented in
455 lakes and ponds, which document clear and predictable trends in $\delta^{18}\text{O}$ and $\Delta^{17}\text{O}$ values of
456 surface waters that follow distinct evaporation slopes (λ) that range from 0.518 to 0.528 and
457 reflect conditions of evaporation in surface waters (e.g., Gázquez et al., 2018; Passey and Ji,
458 2019; Surma et al., 2018). We plot the $\delta^{18}\text{O}_{\text{rsw}}$ and $\Delta^{17}\text{O}_{\text{rsw}}$ values from the Serengeti soils in the
459 context of these evaporation slopes. Assuming that unevaporated soil water is has an isotopic
460 composition similar to spring water ($\delta^{18}\text{O} = -5\text{‰}$, $\Delta^{17}\text{O} = 20$ per meg; Table S13), evaporation
461 slopes of 0.518 – 0.524, that are typical of lakes, capture most of the observed isotopic variation
462 in the Serengeti carbonates (Fig. 7B).

463 The triple oxygen isotopic composition of the dry season soil waters collected from the
464 Serengeti exhibit different trends than the soil waters reconstructed from soil carbonates (Fig.
465 5D). $\Delta^{17}\text{O}_{\text{sw}}$ and $\Delta^{17}\text{O}_{\text{rsw}}$ are indistinct from each other at Ndabaka. At Simba Kopjes, $\Delta^{17}\text{O}_{\text{rsw}}$
466 are largely invariant (Fig. 7B), but $\Delta^{17}\text{O}_{\text{sw}}$ values follow evaporation slopes and are up to 18 per

467 meg lower than $\Delta^{17}\text{O}_{\text{rsw}}$ values (Fig. 5D). In contrast, at Malambo Road and Shifting Sands,
468 $\Delta^{17}\text{O}_{\text{rsw}}$ values are of >50 per meg more negative than $\Delta^{17}\text{O}_{\text{sw}}$ values (Figs. 5D and 7B). As
469 discussed in Section 6.1, isolated collections of soil waters may represent a snapshot of
470 conditions and may be strongly influenced by a recent wetting or drying event. In contrast, the
471 isotopic composition of the soil waters reconstructed from soil carbonates represent average soil
472 conditions over the duration of carbonate formation.

473 The clear association of lower $\Delta^{17}\text{O}_{\text{rsw}}$ values at more arid sites (with lower AI and
474 higher WD) indicates the strong influence of evaporation on the oxygen isotopic composition on
475 soil carbonates in the Serengeti (Figs. 7C, 7D). The observed spatial variability in this transect is
476 important for building a framework for interpreting similar data from the geologic record where
477 we can infer trends through time. Using a suite of measurements including $\delta^{18}\text{O}_{\text{sc}}$, Δ_{47} , and
478 $\Delta^{17}\text{O}_{\text{sc}}$, gives the ability to reconstruct both soil temperatures and $\delta^{18}\text{O}_{\text{rsw}}$ values which can then
479 be used in combination with $\Delta^{17}\text{O}_{\text{rsw}}$ to evaluate the role of evaporation in driving variation in
480 $\delta^{18}\text{O}_{\text{sc}}$. This is an advance over current approaches in which $\delta^{18}\text{O}_{\text{rsw}}$ values are determined from
481 $\delta^{18}\text{O}_{\text{sc}}$ and $T_{\Delta 47}$ measurements (or assumed soil temperature) and are difficult to interpret because
482 the soil water evaporation is unconstrained. For example, there are large differences in the trends
483 of $\delta^{18}\text{O}_{\text{sc}}$ values over the last 4 Ma in eastern Africa; $\delta^{18}\text{O}_{\text{sc}}$ values remains constant over the last
484 4 Ma in the Afar region of Ethiopia but increase by up to 10‰ in the Omo-Turkana Basin in
485 northern Kenya and southern Ethiopia (Levin et al., 2011). We cannot presently evaluate the role
486 of soil water evaporation on these $\delta^{18}\text{O}_{\text{sc}}$ records, but $\Delta^{17}\text{O}_{\text{sc}}$ measurements could provide this
487 constraint.

488 Although $\Delta^{17}\text{O}_{\text{sc}}$ is directly sensitive to evaporation, it may also provide insights into
489 aridity. Aridity is a key variable to understanding the ecosystem pressures on organisms when

490 reconstructing past environments, but it is hard to capture in a proxy as it results from the
491 interplay of rainfall amounts, temperature, and evaporative water loss. The Serengeti soil
492 carbonate data show that $\Delta^{17}\text{O}_{\text{rsw}}$ values track aridity, where $\Delta^{17}\text{O}_{\text{rsw}}$ values decrease by ~ 50
493 per meg between semi-arid and dry sub-humid environments, indicating that there may be a
494 threshold for soil water evaporation between these climate classes (Fig. 7C). We observe a
495 similar shift in $\Delta^{17}\text{O}_{\text{rsw}}$ values when plotted against the water deficit for this region with the most
496 negative $\Delta^{17}\text{O}_{\text{rsw}}$ values at sites with the highest water deficit (Fig. 7D). These data hint at the
497 value of using $\Delta^{17}\text{O}_{\text{rsw}}$ values to track aridity in the geologic record, but it needs to be fully
498 tested in other geographic regions, in additional soil types, ecosystems and in a broader range of
499 climate classes (hyper-arid, arid, and humid).

500

501 **7. Conclusions**

502 The isotopic composition of soil carbonates is a widely used tool for tracking vegetation,
503 temperature, and climate in the geologic record. Our study of soil carbonates sampled along an
504 aridity gradient in the Serengeti, Tanzania, expands the utility of this tool by providing 1) new
505 data on landscape-scale variation in $\delta^{13}\text{C}$, $\delta^{18}\text{O}$ and Δ_{47} values from modern soils in Africa,
506 where there are few isotopic datasets and 2) the first detailed look at the distribution of $\Delta^{17}\text{O}$
507 values in modern soil carbonates and soil waters and how they vary with aridity. We find that the
508 Serengeti $\delta^{13}\text{C}_{\text{sc}}$ values indicate ‘grassland’ within the framework of the fractional woody cover
509 proxy (Cerling et al., 2011), which is consistent with mapped vegetation. The $\delta^{18}\text{O}_{\text{sc}}$ values of
510 the Serengeti soils exhibit a large range (-5 to 4‰), with the highest $\delta^{18}\text{O}_{\text{sc}}$ values at the most
511 arid sites, indicating the importance of increased soil water evaporation on $\delta^{18}\text{O}_{\text{sc}}$ values in arid

512 settings. This trend holds for $\delta^{18}\text{O}_{\text{rsw}}$ values, which we determine from Δ_{47} temperatures values to
513 constrain soil formation temperatures.

514 Our Δ_{47} data indicate that these carbonates record temperatures (ranging from 14 to 29°C
515 with an average of $23 \pm 4^\circ\text{C}$) that span the range of MAAT and MAST and the soil temperatures
516 measured over an 11-month monitoring interval. The *in situ* measurement of soil temperatures
517 and soil modeling indicate that ground heating may increase soil temperature by up to 5°C above
518 MAAT. We observe very little $T_{\Delta 47}$ variation with depth, likely because there is so little annual
519 temperature variation near the equator. Although there are few other $T_{\Delta 47}$ datasets from modern
520 soil carbonates in Africa, the $T_{\Delta 47}$ from the Serengeti are similar to carbonate sampled nearby at
521 Masai Mara Kenya ($18.8 \pm 1.6^\circ\text{C}$), but cooler than the $T_{\Delta 47}$ values from modern soil carbonates in
522 the Afar region of Ethiopia (25–40°C), which is also reflected in measured soil temperatures.
523 Cooler soil temperatures in the Serengeti is likely due a combination of its higher elevation,
524 reduced temperature seasonality in the tropics, and higher precipitation.

525 Finally, our work provides the first systematic view of the distribution of $\Delta^{17}\text{O}$ values in
526 soil carbonates. We observe that $\Delta^{17}\text{O}_{\text{rsw}}$ values decrease by >50 per meg and $\delta^{18}\text{O}_{\text{rsw}}$ values
527 increase by >5‰ from the dry sub-humid sites (Ndabaka, Simba Kopjes, and Banagi) to the
528 semi-arid sites (Shifting Sands and Malambo Road), which likely reflects increased soil water
529 evaporation at the semi-arid sites. Differences in $\Delta^{17}\text{O}_{\text{rsw}}$ and $\delta^{18}\text{O}_{\text{rsw}}$ between sampling sites
530 along the Serengeti transect are far greater than the typical measurement error and show that a
531 combination of $\delta^{18}\text{O}$, Δ_{47} , and $\Delta^{17}\text{O}$ measurements in soil carbonates can be used to detect
532 spatial differences in aridity in modern landscapes. Finally, the ability to constrain the influence
533 of both temperature and evaporation on $\delta^{18}\text{O}_{\text{sc}}$ values will transform interpretations of long-term

534 records of $\delta^{18}\text{O}_{\text{rsw}}$ and allow for direct comparisons between different sites, environments, and
535 time periods, in a way that has previously not been possible.

536

537 **Acknowledgements**

538 This research was conducted under COSTECH Permit #2018-39-NA-2018-17, TANAPA
539 Research Permit #: TNP/HQ/C.10/13, and TAWIRI Permit #: TWRI/RS-342/2016/116. This
540 work was supported by the National Science Foundation [EAR-PF grant #1725621] and the
541 University of Michigan Earth and Environmental Sciences Department. The authors would like
542 to thank Joseph Masoy, Honest Nodoro, and Audax Mabulla for their help with fieldwork and
543 permitting, which made this research possible. The authors would also like to thank Chris
544 Poulsen for the use of the laboratory and Picarro L2130-i and Ryan Horwitz for assistance with
545 analyses. Finally, the authors would like to thank Ian Z. Winklestern, who's discussions and
546 assistance in the laboratory were invaluable to the success of this research. All data are available
547 in the supporting information.

548
549
550
551
552
553
554
555
556
557
558
559
560
561
562
563
564
565

566 **References**

- 567 Allison, G.B., Barnes, C.J., Hughes, M.W., 1983. The distribution of deuterium and ^{18}O in dry
568 soils 2. Experimental. *J. Hydrol.* 64, 377–397. [https://doi.org/10.1016/0022-1694\(83\)90078-](https://doi.org/10.1016/0022-1694(83)90078-1)
569 1
- 570 Aron, P.G., Levin, N.E., Beverly, E.J., Huth, T.E., Passey, B.H., Pelletier, E.M., Poulsen, C.J.,
571 Winkelstern, I.Z., Yarian, D.A., in review. Triple oxygen isotopes in the water cycle. *Chem.*
572 *Geol.*
- 573 Bao, H., Cao, X., Hayles, J.A., 2016. Triple Oxygen Isotopes: Fundamental Relationships and
574 Applications. *Annu. Rev. Earth Planet. Sci* 44, 463–92. [https://doi.org/10.1146/annurev-](https://doi.org/10.1146/annurev-earth-060115-012340)
575 [earth-060115-012340](https://doi.org/10.1146/annurev-earth-060115-012340)
- 576 Barnes, C.J., Allison, G.B., 1983. The distribution of deuterium and O^{18} in dry soils 1. Theory.
577 *J. H* 60, 141–156.
- 578 Bartlett, M.G., Chapman, D.S., Harris, R.N., 2006. A Decade of Ground – Air Temperature
579 Tracking at Emigrant Pass Observatory, Utah. *J. Clim.* 19, 3722–3731.
- 580 Bedaso, Z.K., DeLuca, N.M., Levin, N.E., Zaitchik, B.F., Waugh, D.W., Wu, S.Y., Harman,
581 C.J., Shanko, D., 2020. Spatial and temporal variation in the isotopic composition of
582 Ethiopian precipitation. *J. Hydrol.* 585, 124364.
583 <https://doi.org/10.1016/j.jhydrol.2019.124364>
- 584 Bonifacie, M., Calmels, D., Eiler, J.M., Horita, J., Chaduteau, C., Vasconcelos, C., Agrinier, P.,
585 Katz, A., Passey, B.H., Ferry, J.M., Bourrand, J.J., 2017. Calibration of the dolomite
586 clumped isotope thermometer from 25 to 350 °C, and implications for a universal
587 calibration for all (Ca, Mg, Fe) CO_3 carbonates. *Geochim. Cosmochim. Acta* 200, 255–279.
588 <https://doi.org/10.1016/j.gca.2016.11.028>
- 589 Bowen, G.J., 2020. Gridded maps of the isotopic composition of meteoric waters [WWW
590 Document]. URL <http://www.waterisotopes.org>
- 591 Bowen, G.J., Revenaugh, J., 2003. Interpolating the isotopic composition of modern meteoric
592 precipitation. *Water Resour. Res.* 39, 1–13. <https://doi.org/10.1029/2003WR002086>
- 593 Breecker, D.O., Sharp, Z.D., McFadden, L.D., 2009. Seasonal bias in the formation and stable
594 isotopic composition of pedogenic carbonate in modern soils from central New Mexico,
595 USA. *Bull. Geol. Soc. Am.* 121, 630–640. <https://doi.org/10.1130/B26413.1>
- 596 Cerling, T.E., Quade, J., 1980. Stable carbon and oxygen isotopes in soil carbonates. *Geophys.*
597 *Monogr.* 78, 217–231.
- 598 Cerling, T.E., Wynn, J.G., Andanje, S. a, Bird, M.I., Korir, D.K., Levin, N.E., Mace, W.,
599 Macharia, A.N., Quade, J., Remien, C.H., 2011. Woody cover and hominin environments in
600 the past 6 million years. *Nature* 476, 51–56. <https://doi.org/10.1038/nature10306>
- 601 Dansgaard, W., 1964. Stable isotopes in precipitation. *Tellus* 16, 436–468.
- 602 de Wit, H.A., 1978. Soils and Grassland Types of the Serengeti Plain (Tanzania): Their
603 distributions and interrelations. Wageningen.
- 604 Dennis, K.J., Affek, H.P., Passey, B.H., Schrag, D.P., Eiler, J.M., 2011. Defining an absolute
605 reference frame for “clumped” isotope studies of CO_2 . *Geochim. Cosmochim. Acta* 75,
606 7117–7131. <https://doi.org/10.1016/j.gca.2011.09.025>
- 607 Fick, S.E., Hijmans, R.J., 2017. WorldClim 2: new 1-km spatial resolution climate surfaces for
608 global land areas. *Int. J. Climatol.* 37, 4302–4315. <https://doi.org/10.1002/joc.5086>
- 609 Garziona, C.N., Hoke, G.D., Libarkin, J.C., Withers, S., MacFadden, B., Eiler, J., Ghosh, P.,
610 Mulch, A., 2008. Rise of the Andes. *Science* (80-.). 320, 1304–1307.
611 <https://doi.org/10.1126/science.1148615>

612 Gázquez, F., Morellón, M., Bauska, T., Herwartz, D., Surma, J., Moreno, A., Staubwasser, M.,
613 Valero-Garcés, B., Delgado-Huertas, A., Hodell, D.A., 2018. Triple oxygen and hydrogen
614 isotopes of gypsum hydration water for quantitative paleo-humidity reconstruction. *Earth*
615 *Planet. Sci. Lett.* 481, 177–188. <https://doi.org/10.1016/j.epsl.2017.10.020>

616 Hsieh, J.C.C., Chadwick, O.A., Kelly, E.F., Savin, S.M., 1998. Oxygen isotopic composition of
617 soil water: Quantifying evaporation and transpiration. *Geoderma* 82, 269–293.
618 [https://doi.org/10.1016/S0016-7061\(97\)00105-5](https://doi.org/10.1016/S0016-7061(97)00105-5)

619 Jager, T.J., 1982. *Soils of the Serengeti Woodlands*.

620 Kelson, J.R., Huntington, K.W., Breecker, D.O., Burgener, L.K., Gallagher, T.M., Hoke, G.D.,
621 Petersen, S. V., 2020. A proxy for all seasons? A synthesis of clumped isotope data from
622 Holocene soil carbonates. *Quat. Sci. Rev.* 234, 106259.
623 <https://doi.org/10.1016/j.quascirev.2020.106259>

624 Kim, S.-T., O’Neil, J.R., 1997. Equilibrium and nonequilibrium oxygen isotope effects in
625 synthetic carbonates. *Geochim. Cosmochim. Acta* 61, 3461–3475.
626 [https://doi.org/10.1016/S0016-7037\(97\)00169-5](https://doi.org/10.1016/S0016-7037(97)00169-5)

627 Landais, A., Risi, C., Bony, S., Vimeux, F., Descroix, L., Falourd, S., Bouygues, A., 2010.
628 Combined measurements of 17O excess and d -excess in African monsoon precipitation:
629 Implications for evaluating convective parameterizations. *Earth Planet. Sci. Lett.* 298, 104–
630 112. <https://doi.org/10.1016/j.epsl.2010.07.033>

631 Levin, N., Brown, F.H., Behrensmeyer, A.K., Bobe, R., Cerling, T.E., 2011. Paleosol carbonates
632 from the Omo Group: Isotopic records of local and regional environmental change in East
633 Africa. *Palaeogeogr. Palaeoclimatol. Palaeoecol.* 307, 75–89.

634 Levin, N.E., Zipser, E.J., Ceding, T.E., 2009. Isotopic composition of waters from Ethiopia and
635 Kenya: Insights into moisture sources for eastern Africa. *J. Geophys. Res. Atmos.* 114, 1–
636 13. <https://doi.org/10.1029/2009JD012166>

637 Li, S., Levin, N.E., Soderberg, K., Dennis, K.J., Caylor, K.K., 2017. Triple oxygen isotope
638 composition of leaf waters in Mpala, central Kenya. *Earth Planet. Sci. Lett.* 468, 38–50.
639 <https://doi.org/10.1016/j.epsl.2017.02.015>

640 Loomis, S.E., Russell, J.M., Verschuren, D., Morrill, C., De Cort, G., Sinninghe Damsté, J.S.,
641 Olago, D., Eggermont, H., Alayne Street-Perrott, F., Kelly, M.A., 2017. The tropical lapse
642 rate steepened during the Last Glacial Maximum. *Sci. Adv.* 3, 1–7.
643 <https://doi.org/10.1126/sciadv.1600815>

644 Lüdecke, T., Kullmer, O., Wacker, U., Sandrock, O., Fiebig, J., Schrenk, F., Mulch, A., 2018.
645 Dietary versatility of Early Pleistocene hominins. *Proc. Natl. Acad. Sci.* 201809439.
646 <https://doi.org/10.1073/pnas.1809439115>

647 Luz, B., Barkan, E., 2010. Variations of $17\text{O}/16\text{O}$ and $18\text{O}/16\text{O}$ in meteoric waters. *Geochim.*
648 *Cosmochim. Acta* 74, 6276–6286. <https://doi.org/10.1016/j.gca.2010.08.016>

649 Middleton, N., Thomas, D. (Eds.), 1997. *World Atlas of Desertification*, 2nd ed. Hodder Arnold,
650 London.

651 Miller, M.F., 2002. Isotopic fractionation and the quantification of 17O anomalies in the oxygen
652 three-isotope system: an appraisal and geochemical significance. *Geochim. Cosmochim.*
653 *Acta* 66, 1881–1889.

654 Odada, E.O., 2001. Stable isotopic composition of East African lake waters (No. IAEA-
655 TECDOC--1206).

656 Otte, I., Detsch, F., Gütlein, A., Scholl, M., Kiese, R., Appelhans, T., Nauss, T., 2017.
657 Seasonality of stable isotope composition of atmospheric water input at the southern slopes

658 of Mt. Kilimanjaro, Tanzania. *Hydrol. Process.* 31, 3932–3947.
659 <https://doi.org/10.1002/hyp.11311>

660 Passey, B.H., Hu, H., Ji, H., Montanari, S., Li, S., Henkes, G.A., Levin, N.E., 2014. Triple
661 oxygen isotopes in biogenic and sedimentary carbonates. *Geochim. Cosmochim. Acta* 141,
662 1–25. <https://doi.org/10.1016/j.gca.2014.06.006>

663 Passey, B.H., Ji, H., 2019. Triple oxygen isotope signatures of evaporation in lake waters and
664 carbonates: A case study from the western United States. *Earth Planet. Sci. Lett.* 518, 1–12.
665 <https://doi.org/10.1016/j.epsl.2019.04.026>

666 Passey, B.H., Levin, N.E., Cerling, T.E., Brown, F.H., Eiler, J.M., Turekian, K.K., 2010. High-
667 temperature environments of human evolution in East Africa based on bond ordering in
668 paleosol carbonates. *Proc. Natl. Acad. Sci. U. S. A.* 107, 1–5.
669 <https://doi.org/10.1073/pnas.1001824107>

670 Quade, J., Eiler, J., Daëron, M., Achyuthan, H., 2013. The clumped isotope geothermometer in
671 soil and paleosol carbonate. *Geochim. Cosmochim. Acta* 105, 92–107.
672 <https://doi.org/10.1016/j.gca.2012.11.031>

673 Quade, J., Rech, J., Latorre, C., Betancourt, J., Gleeson, E., Kalin, M., 2007. Soils at the
674 hyperarid margin: The isotopic composition of soil carbonate from the Atacama Desert,
675 Northern Chile. *Geochim. Cosmochim. Acta* 71, 3772–3795.
676 <https://doi.org/10.1016/j.gca.2007.02.016>

677 Rech, J.A., Currie, B.S., Jordan, T.E., Riquelme, R., Lehmann, S.B., Kirk-Lawlor, N.E., Li, S.,
678 Gooley, J.T., 2019. Massive middle Miocene gypsic paleosols in the Atacama Desert and
679 the formation of the Central Andean rain-shadow. *Earth Planet. Sci. Lett.* 506, 184–194.
680 <https://doi.org/10.1016/j.epsl.2018.10.040>

681 Reed, D.N., Anderson, T.M., Dempewolf, J., Metzger, K., Serneels, S., 2009. The spatial
682 distribution of vegetation types in the Serengeti ecosystem: The influence of rainfall and
683 topographic relief on vegetation patch characteristics. *J. Biogeogr.* 36, 770–782.
684 <https://doi.org/10.1111/j.1365-2699.2008.02017.x>

685 Rozanski, K., Araguas-Araguas, L., Gonfiantini, R., 1996. Isotope patterns of precipitation in the
686 East African region, in: *The Limnology, Climatology and Paleoclimatology of the East*
687 *African Lakes*. pp. 79–93.

688 Salomons, W., Goudie, A., Mook, W.G., 1978. Isotopic Composition of Calcrete Deposits from
689 Europe, Africa and India. *Earth Surf. Process.* 3, 43–57.

690 Schoenemann, S.W., Schauer, A.J., Steig, E.J., 2013. Measurement of SLAP2 and GISP d17O
691 and proposed VSMOW-SLAP normalization for d17O and 17Oexcess. *Rapid Commun.*
692 *Mass Spectrom.* 27, 582–590. <https://doi.org/10.1002/rcm.6486>

693 Shukla, M.K., 2014. *Soil Physics: An Introduction*. Taylor & Francis Group, Boca Raton, FL.

694 Soil Survey Staff, 2014. *Illustrated Guide to Soil Taxonomy*, 1.0. ed. USDA NRCS, Lincoln
695 Nebraska.

696 Surma, J., Assonov, S., Herwartz, D., Voigt, C., Staubwasser, M., 2018. The evolution of 17O-
697 excess in surface water of the arid environment during recharge and evaporation. *Sci. Rep.*
698 8, 4972. <https://doi.org/10.1038/s41598-018-23151-6>

699 Wang, Z., Schauble, E.A., Eiler, J.M., 2004. Equilibrium thermodynamics of multiply
700 substituted isotopologues of molecular gases. *Geochim. Cosmochim. Acta* 68, 4779–4797.
701 <https://doi.org/10.1016/j.gca.2004.05.039>

702 West, A.G., Patrickson, S.J., Ehleringer, J.R., 2006. Water extraction times for plant and soil
703 materials used in stable isotope analysis. *Rapid Commun. Mass Spectrom.* 20, 1317–1321.

704 <https://doi.org/10.1002/rcm.2456>
705 Yin, X., Nicholson, S.E., 1998. The water balance of Lake Victoria. *Hydrol. Sci. J.*
706 Young, E.D., Galy, A., Nagahara, H., 2002. Kinetic and equilibrium mass-dependant isotope
707 fractionation laws in nature and their geochemical and cosmochemical significance.
708 *Geochim. Cosmochim. Acta* 66, 1095–1104. [https://doi.org/10.1016/S0016-7037\(01\)00832-](https://doi.org/10.1016/S0016-7037(01)00832-8)
709 8
710
711
712
713
714
715
716
717
718
719
720
721
722
723
724
725
726
727
728
729
730
731
732
733
734
735
736
737
738
739
740
741
742
743
744
745
746
747
748
749

750 **Figures**

751

752 **Figure 1.** Location map of the study area. (a) Location of the Serengeti in Africa and the position
753 of important climatological features: the intertropical convergence zone (ITCZ) during June,
754 July, August (JJA) and December, January, February (DJF). (b) Location of parks where work
755 was conducted in the Serengeti-Masai Mara Ecosystem outlined in gray over a map of the
756 Aridity Index (MAP/PET) for northern Tanzania and southern Kenya. The locations of water
757 sample collection sites and soil profiles are also indicated. The warmer to cooler colors of the
758 soil profiles sites across the transect are consistent throughout Figures 3-5.

759

760 **Figure 2.** (a) Measured soil temperatures are plotted and smoothed to a daily average over an 11
761 month period and are contrasted with monthly average air temperature from Fick and Hijmans
762 (2017). Color scheme is consistent with Figure 1. (b) Plot of $T_{\Delta 47}$ versus depth. The gray box
763 indicates the range of measured soil temperatures from all sites and all depths. The is the range
764 of modeled soil temperature $+5^{\circ}\text{C}$ to account for ground heating due to incident solar radiation.
765 See Section 6.2 and Fig. 3 for explanation. Errors bars for Δ_{47} use the propagated SE of \pm
766 0.015%.

767

768 **Figure 3.** (a-d) Comparison of measured soil temperature, monthly average air temperature, and
769 modeled soil temperature from Ndabaka in the northwest and Naabi Hill in the southeast. (a)
770 Ndabaka site at 20 cm depth (b) Naabi Hill at 20 cm depth (c) Ndabaka at 150 cm depth (d)
771 Naabi Hill at 150 cm depth (e-f) Results from the modeling of Ndabaka and Naabi Hill plotted
772 with depth. The MAAT is shown by the black dashed line and MAST indicated by the solid
773 black line. (e) The range of modeled temperatures are plotted in light blue and the range of
774 measured values at 150 cm depth are plotted in dark blue. (e) The range of modeled temperatures
775 are plotted in light orange and the range of measured values at 150 cm depth are plotted in dark
776 orange. Note the $+5^{\circ}\text{C}$ which illustrates the effect of ground heating due to incident solar
777 radiation, which is not included in this simple model, but can have a significant effect on soil
778 temperatures (see text for additional discussion).

779

780 **Figure 4.** (a) Monthly and mean values for precipitation, $\delta^{18}\text{O}$ and δD from the Online Isotopes
781 in Precipitation Calculator (OPIC) (Bowen, 2020; Bowen and Revenaugh, 2003)) from the
782 transect endmembers (Ndabaka and Malambo Road) and midpoint (Makoma) of the transect.
783 Color scheme is consistent with Figure 3. (b) Plot of $\delta^{18}\text{O}$ and δD from all waters analyzed for
784 this study with the Global Meteoric Water Line (GMWL) shown in black, African Meteoric
785 Water Line (AMWL) in red (Rozanski et al., 1996), and local meteoric water line (LMWL) in
786 green (Otte et al., 2017). (c) Plot of $\delta^{18}\text{O}$ and d-excess from all waters analyzed for this study.
787 Errors for $\delta^{18}\text{O}$ and δD are smaller than symbols.

788

789 **Figure 5.** (a) Plot of $\Delta^{17}\text{O}$ and d-excess with symbols colored by water type. (b) Plot of $\Delta^{17}\text{O}$
790 and d-excess of soil water ($\Delta^{17}\text{O}_{\text{sw}}$ and $\text{d-excess}_{\text{sw}}$) with symbols colored by soil site (c) Plot of
791 $\delta^{18}\text{O}$ and $\Delta^{17}\text{O}$ with symbols colored by water type. (d) Plot of $\delta^{18}\text{O}$ and $\Delta^{17}\text{O}$ of soil water
792 ($\delta^{18}\text{O}_{\text{sw}}$ and $\Delta^{17}\text{O}_{\text{sw}}$) with a λ value (0.518) plotted for reference. Symbols colored by site. Refer
793 to Figure 1 for locations. (a-d) $\Delta^{17}\text{O}$ typical error of ± 15 per meg indicated. $\delta^{18}\text{O}$ and d-excess
794 error less than width of symbol.

795

796 **Figure 6.** (a) Plot of $\delta^{13}\text{C}$ and $\delta^{18}\text{O}$ of soil carbonates ($\delta^{13}\text{C}_{\text{sc}}$, $\delta^{18}\text{O}_{\text{sc}}$) from this study along with
797 the published data from modern soil carbonates available from elsewhere in Africa. Eastern
798 Africa data are from Kenya, Ethiopia, and Tanzania and the rest of the data are from Libya and
799 South Africa (Cerling and Quade, 1980; Passey et al., 2010; Salomons et al., 1978). The percent
800 fractional woody cover and vegetation classification are noted by different background colors
801 based on $\delta^{13}\text{C}_{\text{sc}}$ after Cerling et al. (2011). (b) $\delta^{18}\text{O}_{\text{sc}}$ plotted against depth. (c) $\delta^{18}\text{O}_{\text{sc}}$ plotted
802 against depth.

803 **Figure 7.** (a) Plot of $\delta^{18}\text{O}_{\text{rsw}}$ (calculated using the $\delta^{18}\text{O}_{\text{sc}}$ values and $T_{\Delta 47}$ from Table 6) versus
804 modeled mean annual $\delta^{18}\text{O}$ of meteoric water from OPIC (Bowen, 2020; Bowen and Revenaugh,
805 2003). (b) Plot of $\delta^{18}\text{O}$ and $\Delta^{17}\text{O}$ of reconstructed soil water ($\delta^{18}\text{O}_{\text{rsw}}$ and $\Delta^{17}\text{O}_{\text{rsw}}$) with typical
806 evaporation slopes, λ , plotted for reference assuming two different starting compositions of
807 unevaporated soil water of ($\Delta^{17}\text{O} = 20$ per meg and $\delta^{18}\text{O} = -7\text{‰}$ and -5‰). (c) Aridity Index
808 (MAP/PET) versus $\Delta^{17}\text{O}_{\text{rsw}}$. (d) Water Deficit (PET - MAP) versus $\Delta^{17}\text{O}_{\text{rsw}}$. The x-axis is
809 reversed so that the highest water deficits align with the greatest aridity in Figure 7C.

810

811 **Tables**

812

813 **Table 1.** Location, soil, and climate information

814

815 **Table 2.** Summary statistics from Hobo temperature logger record.

816

817 **Supporting Information**

818

819 **Figure S1.** (a) Schematic diagram where $\Delta^{17}\text{O}$ represents the deviation of $\delta^{17}\text{O}$ and $\delta^{18}\text{O}$ from
820 the equilibrium Global Meteoric Water Line (GMWL; $\lambda_{\text{ref}} = 0.528$). (b) Evaporation should
821 cause a decrease in $\Delta^{17}\text{O}$ values and an increase in $\delta^{18}\text{O}$ compared to the observed range of
822 global precipitation. See Section 2. for explanation of triple oxygen isotope notation. (c)
823 Schematic illustrating how reconstructed water values for $\delta^{18}\text{O}$ and $\Delta^{17}\text{O}$ are calculated.

824

825 **Figure S2.** Representative examples of the soils described and carbonate morphologies identified
826 in this study. (a) Sandy Inceptisol from the most arid region of the Serengeti, Shifting Sands. (b)
827 Mollisol with abundant calcium carbonate in the profile and illuviated clay that the base from the
828 Kirawira site. (c) Alfisol with significant accumulation of sesquioxides and abundant FeMn
829 nodules from the Kemarishe site. (d) Mollisol with vertic properties including significant cracks
830 extending to 40 cm depth and pedogenic slickensides. The Ndabaka site was only soil profile
831 with pedogenic slickensides (e) Example of the range of sizes of pedogenic carbonate nodules
832 present at the same depth at Ndabaka site. (f) Highly abundant carbonate nodules from the Simba
833 Kopjes site with a popcorn like texture found at many of the sites. (g) Highly calcareous matrix
834 and abundant soil carbonates from the Musabi site. (h) Carbonate coatings on a cobble of highly
835 weathered igneous rock from Shifting Sands site. (i) Coalesced nodules forming a petrocalcic
836 horizon at the Banagi site.

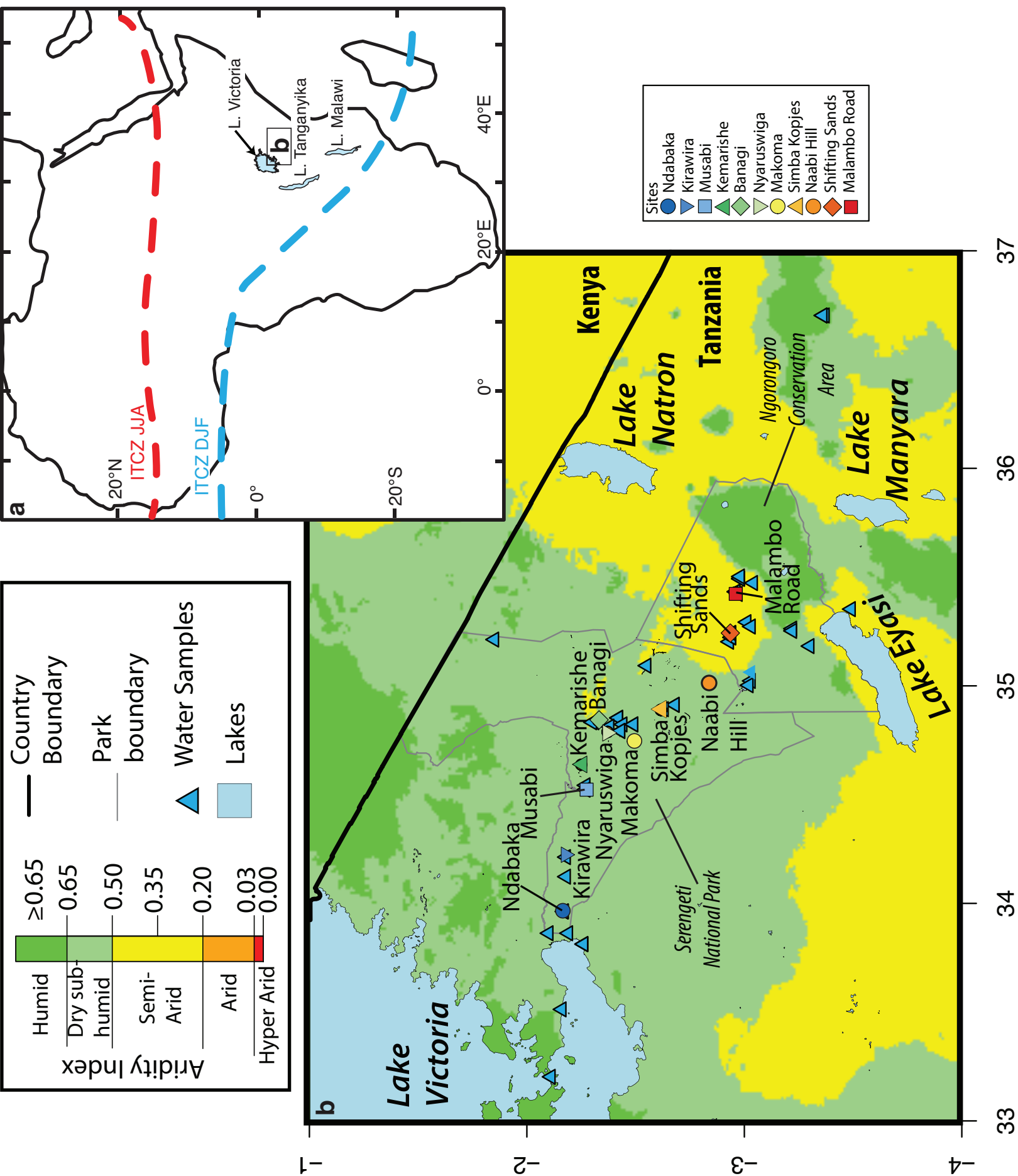
837

838 **Figure S3.** (a) $\Delta^{17}\text{O}_{\text{sw}}$ plotted with depth. (b) $\Delta^{17}\text{O}_{\text{rsw}}$ plotted with depth. (c) $\delta^{18}\text{O}_{\text{sw}}$ plotted with
839 depth. (d) $\delta^{18}\text{O}$ plotted with depth. (e) d-excess plotted with depth. (a-e) colored by site.

840

841 **Table S1.** Soil temperature logger data.
842
843 **Table S2.** Carbon and oxygen isotopic data, description of carbonate morphology, and sampling
844 procedure.
845
846 **Table S3.** Summary statistics of carbon and oxygen isotopes.
847
848 **Table S4.** Raw and corrected clumped isotope data for samples and standards.
849
850 **Table S5.** Summary of clumped and triple oxygen isotopic data organized by site and depth in
851 soil.
852
853 **Table S6.** Standards summary and pooled standard deviation for triple oxygen isotopes and
854 clumped isotopes.
855
856 **Table S7.** Triple oxygen isotope raw and corrected data for Reactor 4.2.
857
858 **Table S8.** Triple oxygen isotope raw and corrected data for Reactor 5.
859
860 **Table S9.** Triple oxygen isotope raw and corrected data for Reactor 6.
861
862 **Table S10.** Triple oxygen isotope raw and corrected data for Reactor 7.
863
864 **Table S11.** Triple oxygen isotope raw and corrected data for Reactor 8.
865
866 **Table S12.** Physical descriptions of soils.
867
868 **Table S13.** $\delta^{18}\text{O}$, δD , and $\Delta^{17}\text{O}$ water data. Values in ‰ VSMOW-SLAP unless otherwise
869 indicated.
870
871 **Table S14.** Pairwise comparison of the measured soil temperature means.
872

Figure 1



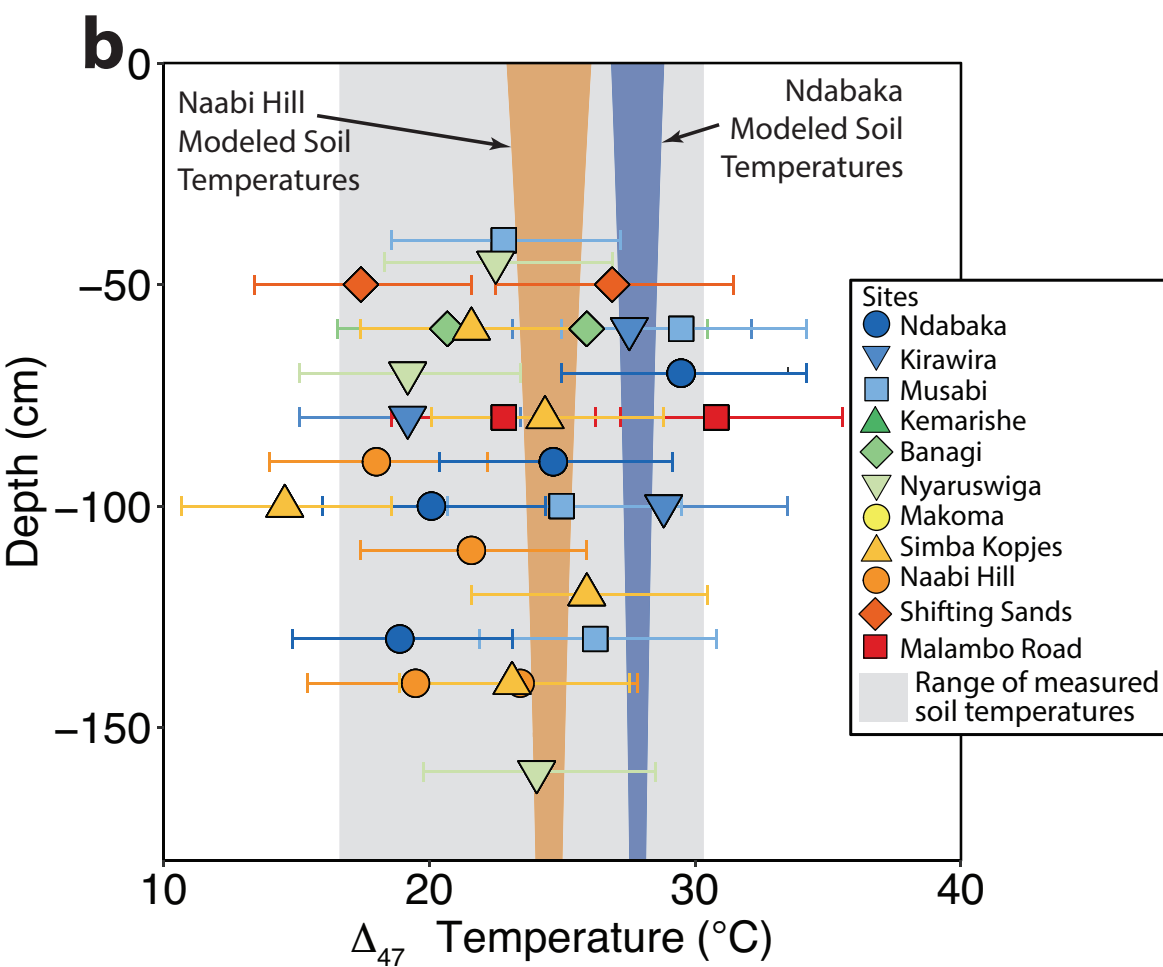
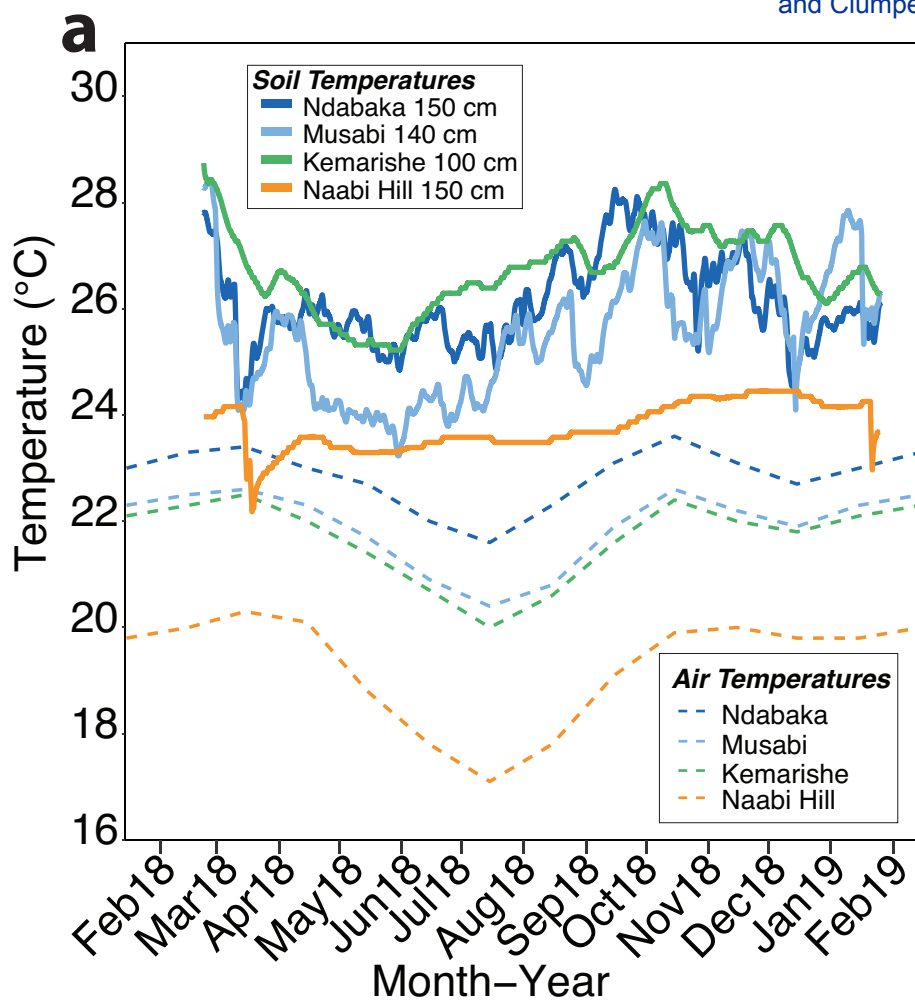


Figure 3

[Click here to access/download/Figure3/Soil_Temperature_Modeling.epi](#)

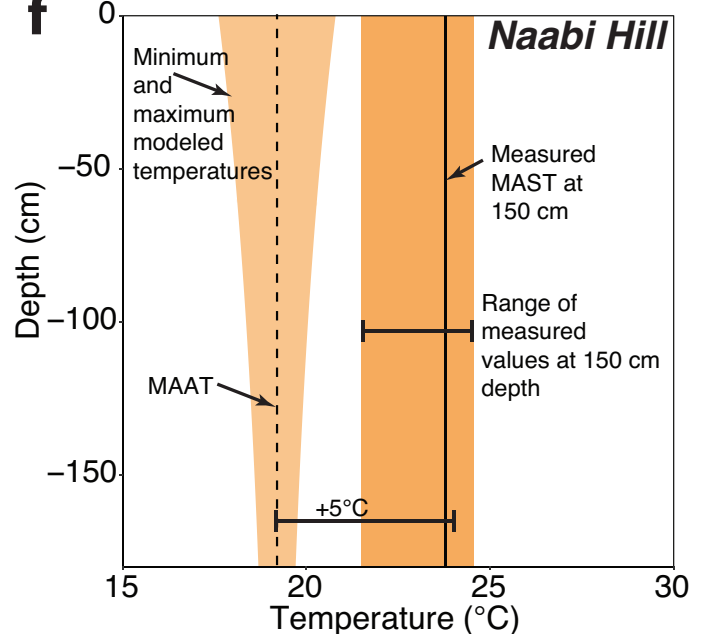
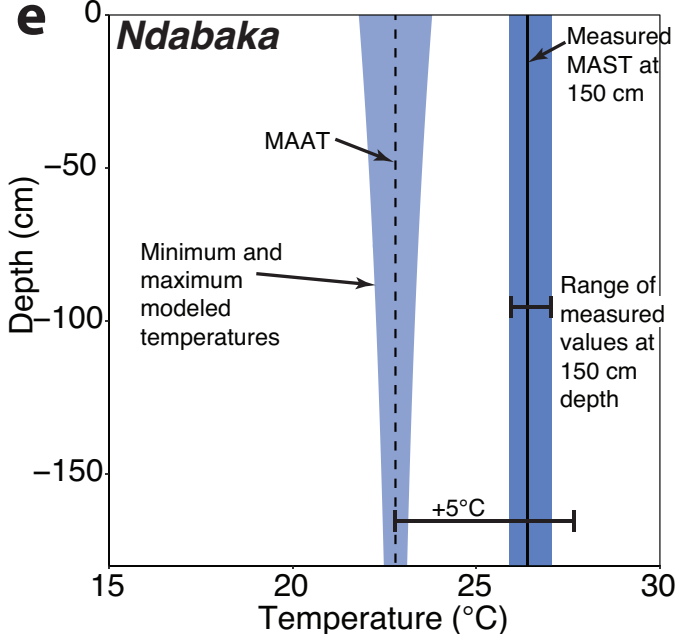
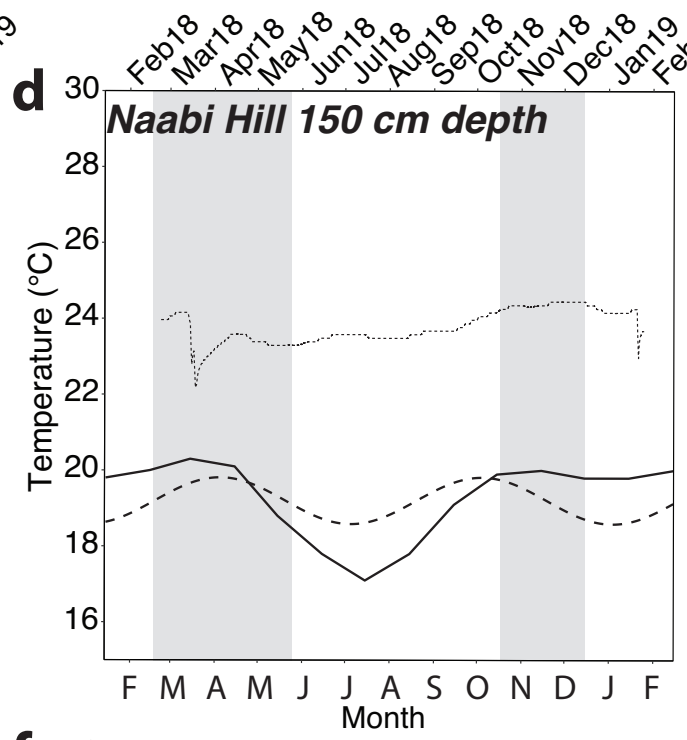
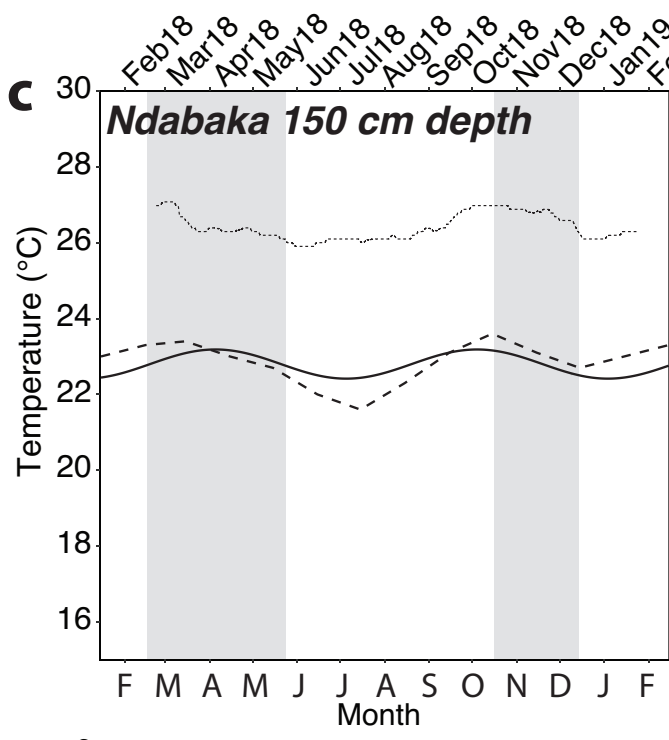
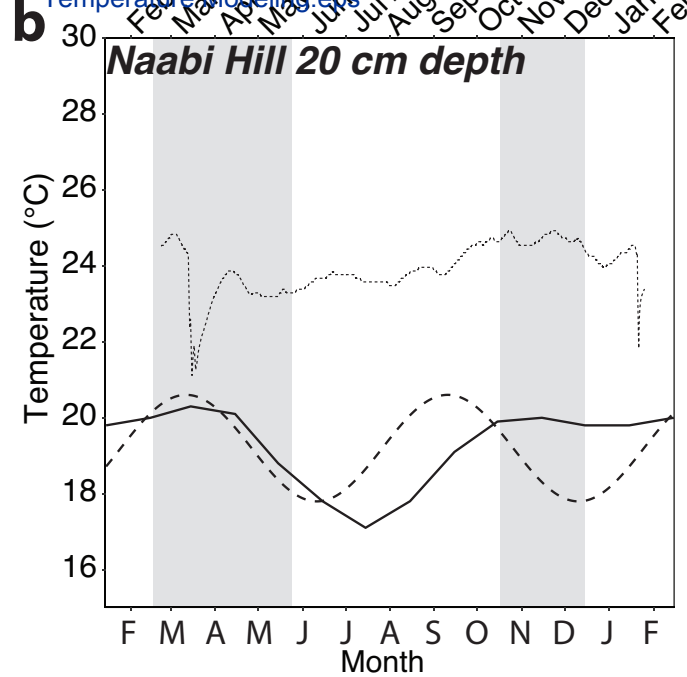
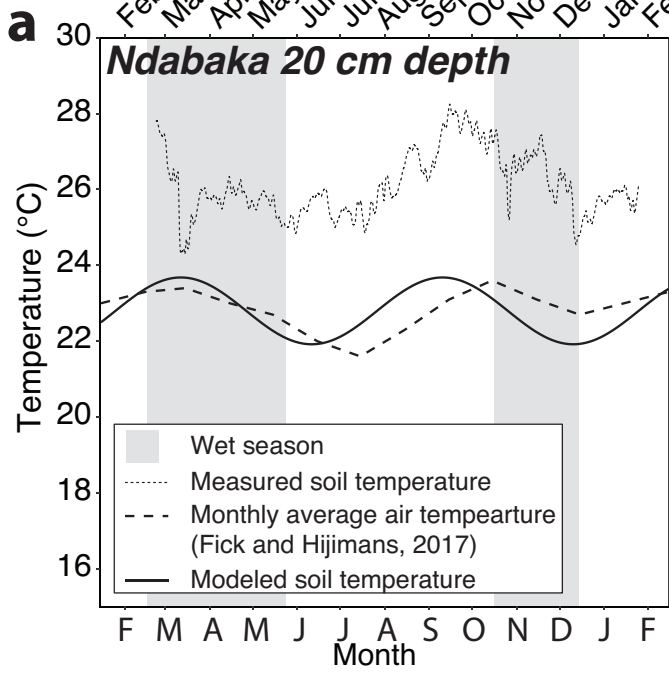
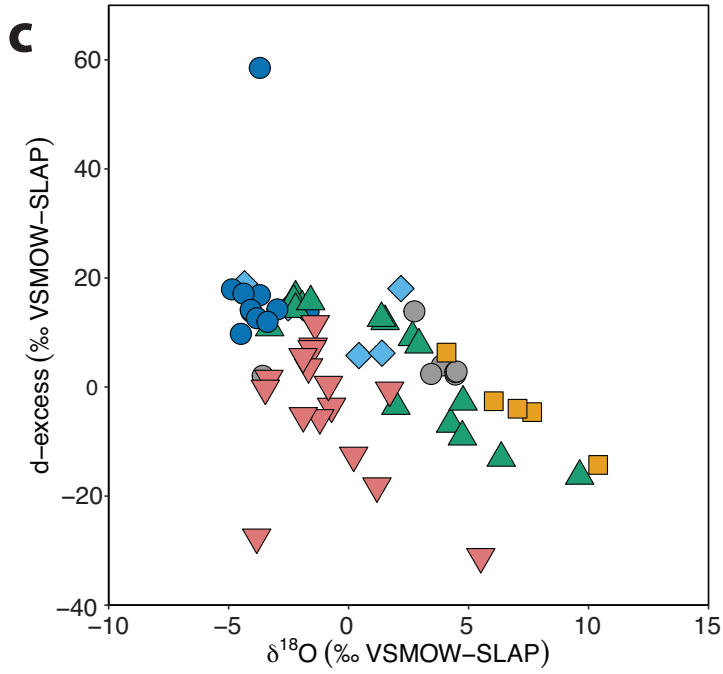
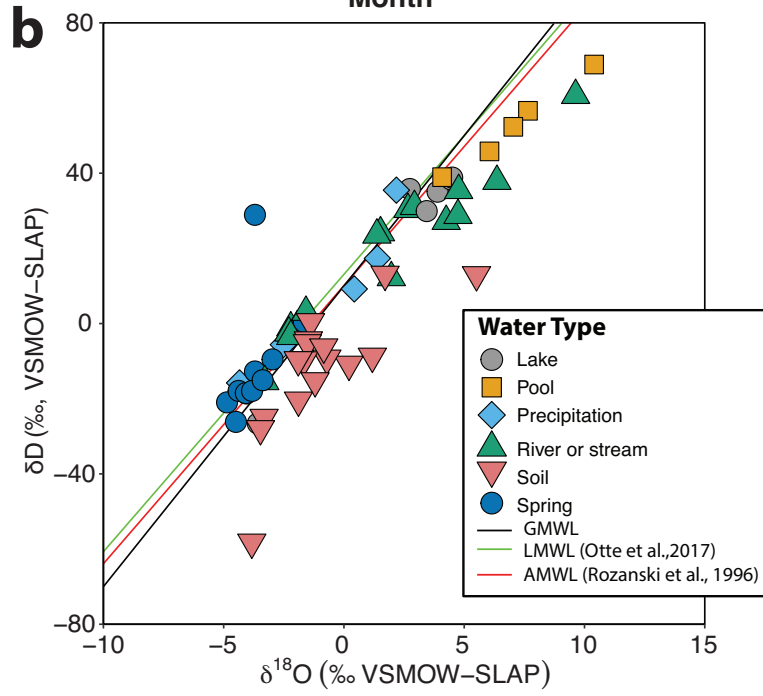
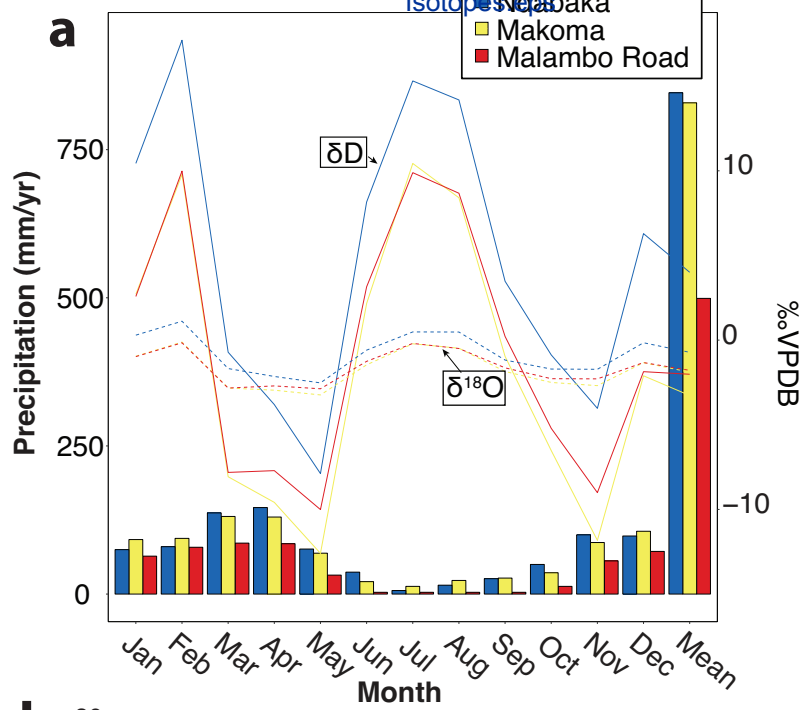
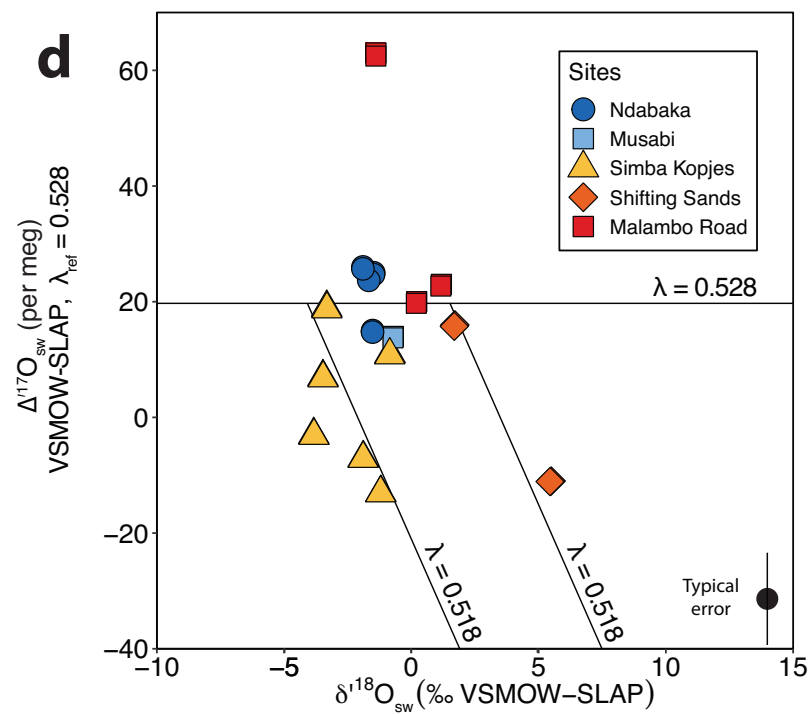
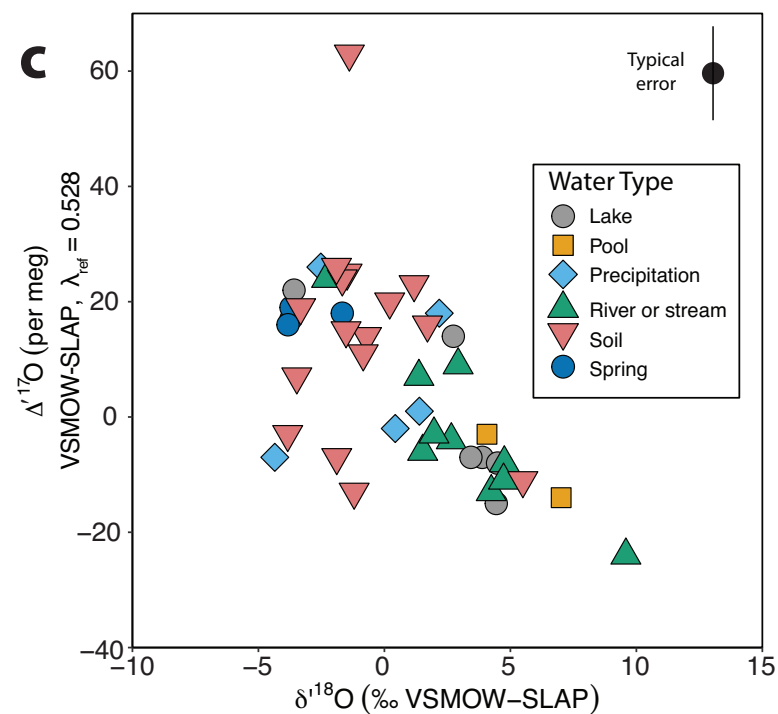
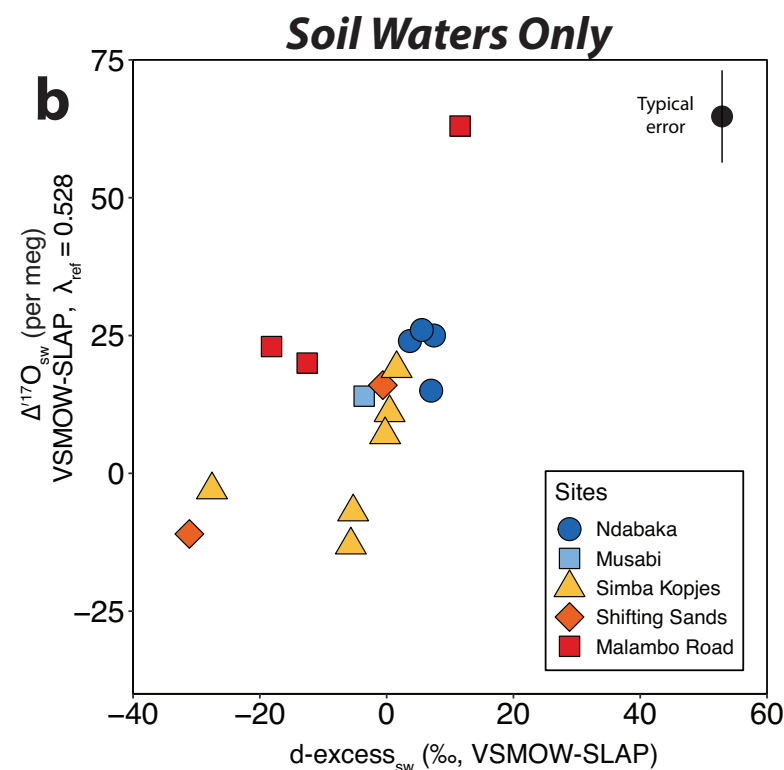
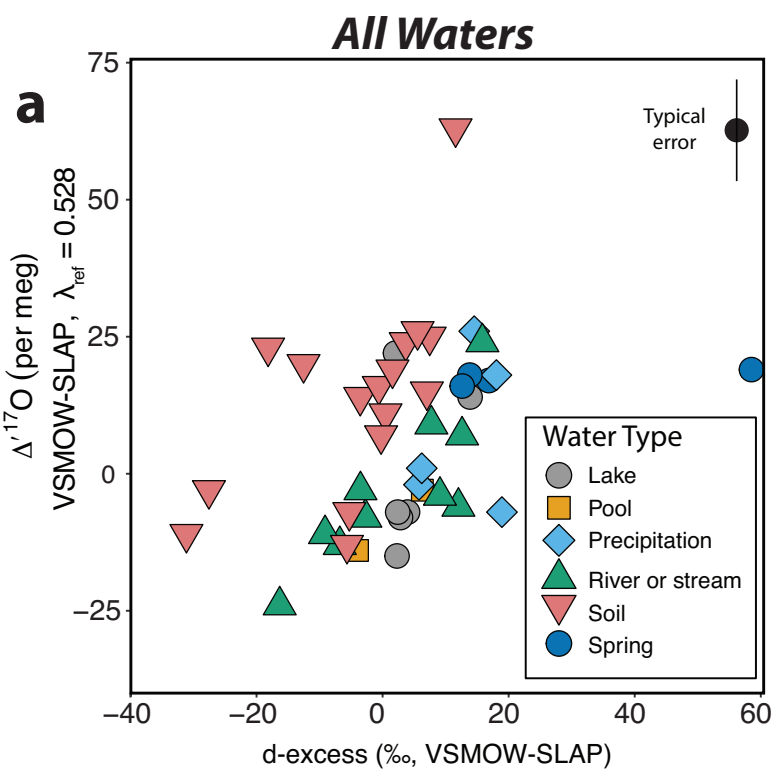
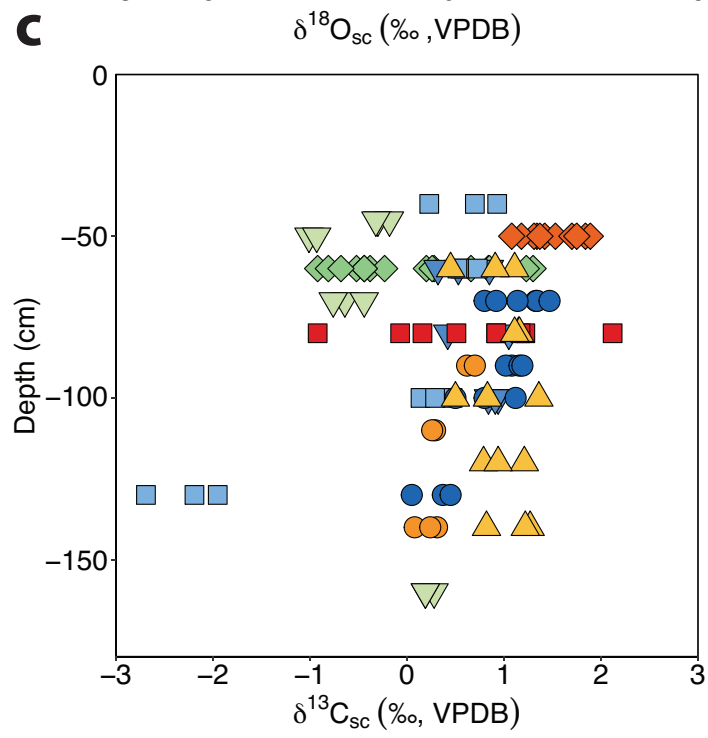
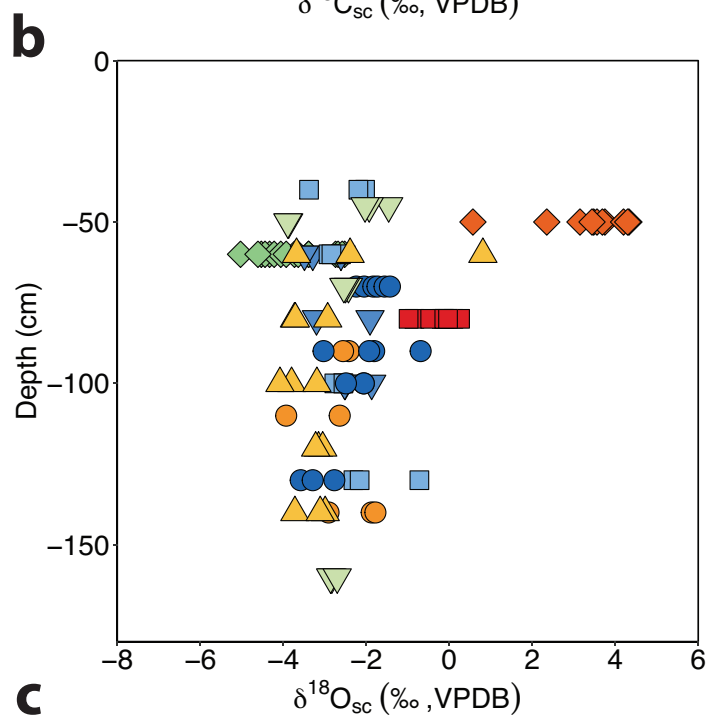
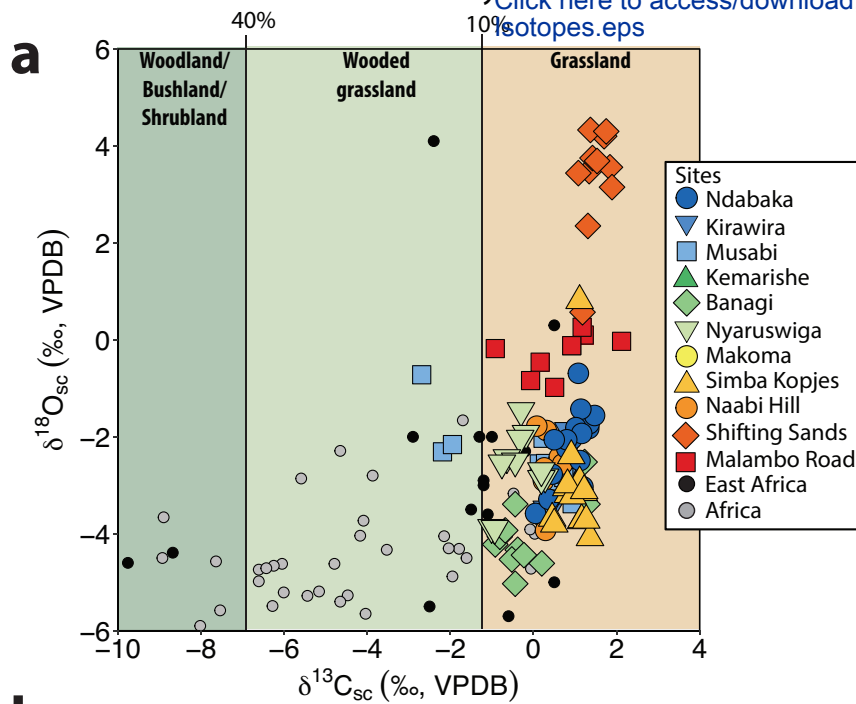


Figure 4







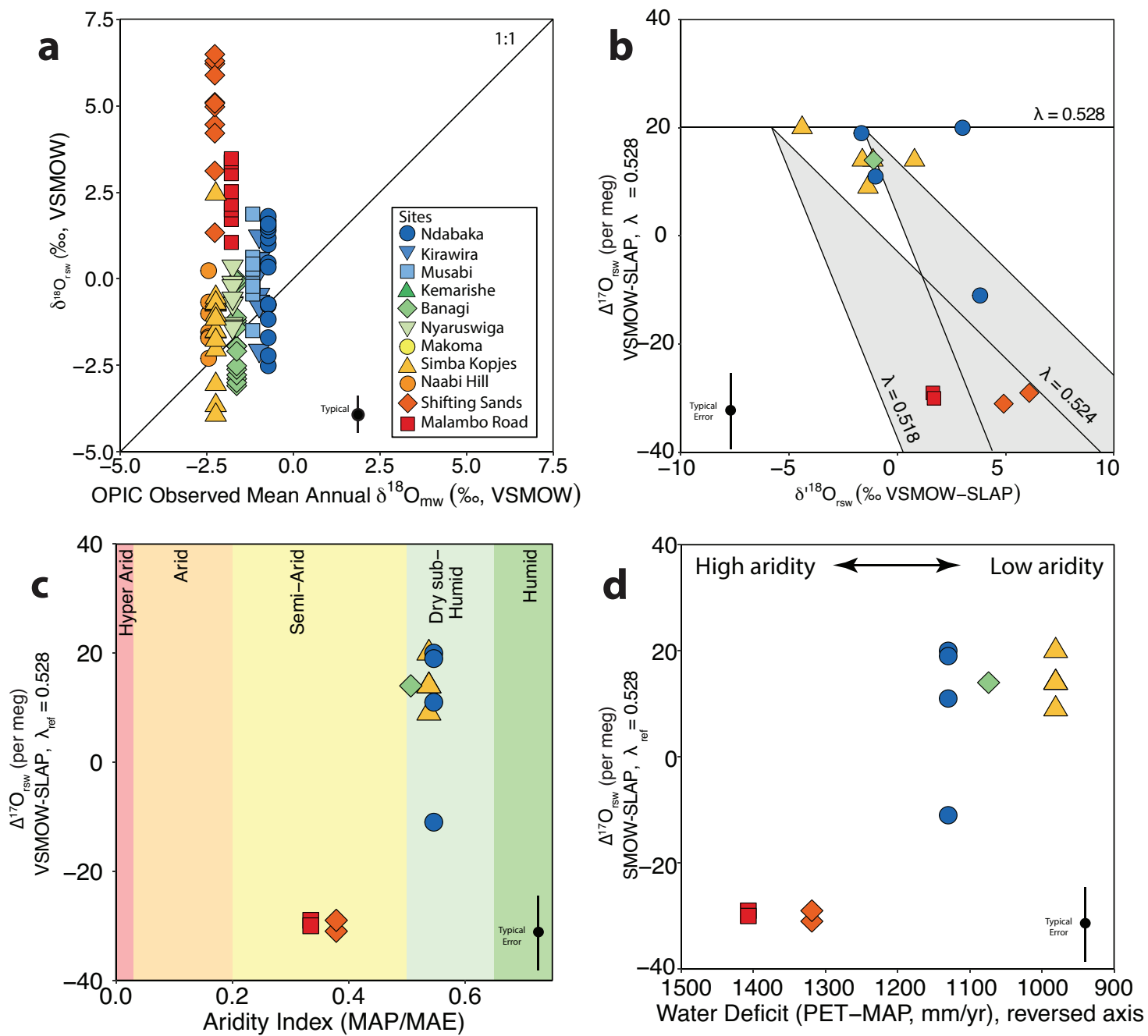


Table 1: Location, soil, and climate information.

Site	Latitude	Longitude ^a	Elevation (masl) ^b	Vegetation ^c	Soil Order ^d	MAT (°C) ^e	MTW Q (°C) ^e	MAP (mm/yr) ^e	PET (mm/yr) ^f	AI ^f	WD (mm/yr) ^f
Malambo Road	-2.9603	35.4364	1354	Dense grassland	Inceptisol	20.9	22.0	499	1583	0.3	1084
Shifting Sands	-2.9355	35.2473	1549	Dense shrubbed grassland	Inceptisol	19.8	20.9	558	1521	0.3	963
Naabi Hill	-2.8396	35.0205	1677	Closed shrubbed grassland	Mollisol	19.2	20.1	734	1486	0.5	752
Simba	-2.6169	34.8966	1637	Dense to closed grassland	Mollisol	19.6	20.5	805	1521	0.5	716
Kopjes	-2.6169	34.8966	1637	Closed treed shrubland	Mollisol	19.6	20.5	805	1521	0.5	716
Makoma	-2.4930	34.7544	1549	Closed treed shrubland	Inceptisol	20.2	21.0	829	1560	0.5	731
Nyaruswiga	-2.3496	34.8263	1451	Open treed grassland to closed grassland	Mollisol	20.8	21.6	832	1613	0.5	781
Banagi	-2.3290	34.8478	1425	Mixed open grassland to woodland	Inceptisol	20.9	21.8	819	1622	0.5	803
Kemarishe	-2.2498	34.6448	1315	Open grassed woodland	Alfisol	21.6	22.3	834	1659	0.5	825
Musabi	-2.2719	34.5339	1278	Closed grassland	Mollisol	21.9	22.5	830	1659	0.5	829
Kirawira	-2.1883	34.2322	1215	Dense to closed grassland	Mollisol	22.4	22.9	838	1655	0.5	817
Ndabaka	-2.1654	33.9734	1153	Dense to closed grassland	Vertic Mollisol	22.8	23.2	846	1642	0.5	796

^adatum WGS 1984

^bmeters above sea level

^cVegetation from Reed et al. (2009)

^dSoil Order identified based on field observations and climate, to provide a general understanding of soil type, but is not intended to be an absolute USDA soil classification

^eMAT = Mean Annual Temperature, MTWQ = Mean Temperature Warmest Quarter, MAP = Mean Annual Precipitation from Fick and Hijmans (2017)

^fPET= Potential Evapotranspiration, AI = Aridity Index, and WD = Water Deficit from Zomer et al. (2007,2008).

Table 2: Summary statistics from Hobo temperature logger record.

Site	Depth (cm)	Min T (°C)	Max T (°C)	Mean T (°C)	SD	Variance
Ndabaka	20	24.16	28.46	26.11	0.86	0.74
Ndabaka	80	25.51	27.66	26.41	0.58	0.34
Ndabaka	150	25.90	27.07	26.40	0.35	0.12
Musabi	40	21.57	28.46	25.51	1.19	1.42
Musabi	140	24.93	27.27	25.90	0.58	0.33
Kamarishe	30	23.48	30.15	26.39	1.38	1.89
Kamarishe	100	25.22	29.25	26.73	0.78	0.62
Naabi Hill	20	16.71	28.36	24.13	1.73	3.00
Naabi Hill	90	19.95	24.93	23.93	0.68	0.46
Naabi Hill	150	21.95	24.55	23.78	0.44	0.20



[Click here to access/download](#)

Supplementary material for online publication only
Figure S1 - 17O Schematic.eps

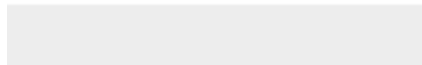




[Click here to access/download](#)

Supplementary material for online publication only

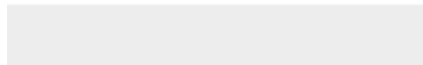
Figure S2 - Field Photos.jpg





[Click here to access/download](#)

Supplementary material for online publication only
Figure S3 - Waters by depth.eps

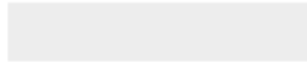




[Click here to access/download](#)

Supplementary material for online publication only

Figure S4 - 17O carb depth.eps





[Click here to access/download](#)

Supplementary material for online publication only
Table S1- Soil Temperatures.xlsx





[Click here to access/download](#)

Supplementary material for online publication only
Table S2 - Traditional Stable Isotopes.xlsx





[Click here to access/download](#)

Supplementary material for online publication only
Table S3 - Summary C and O.xlsx





[Click here to access/download](#)

Supplementary material for online publication only
Table S4 - Clumped Isotope Raw Data.xlsx





[Click here to access/download](#)

Supplementary material for online publication only
Table S5 - Triple and Clumped.xlsx





[Click here to access/download](#)

Supplementary material for online publication only
Table S6- Standard Precision.xlsx





[Click here to access/download](#)

Supplementary material for online publication only

Table S7 - Reactor 4.2.xlsx





[Click here to access/download](#)

Supplementary material for online publication only
Table S8 - Reactor 5.xlsx





[Click here to access/download](#)

Supplementary material for online publication only

Table S9 - Reactor 6.xlsx





[Click here to access/download](#)

Supplementary material for online publication only

Table S10 - Reactor 7.xlsx





[Click here to access/download](#)

Supplementary material for online publication only

Table S11 - Reactor 8.xlsx





[Click here to access/download](#)

Supplementary material for online publication only
Table S12 - Soil Descriptions.xlsx





Click here to access/download

Supplementary material for online publication only
Table S13 - Water Isotope Data.xlsx





[Click here to access/download](#)

Supplementary material for online publication only
Table S14 - Pairwise t-test.xlsx

